Title: Direct quantification of condensate material properties in live cells reveals the regulation of synapsin condensates viscoelasticity by alpha-synuclein

Authors: Huan Wang[1], Christian Hoffmann[2], Johannes V. Tromm[2], Xiao Su[3,4], Jordan Elliott[1], Han Wang[2], Jean Baum[1], Zhiping P. Pang[3,4], Dragomir Milovanovic[2,5,6]*, Zheng Shi[1,7]*

[1] Department of Chemistry and Chemical Biology, Rutgers University, Piscataway, NJ 08854, USA. [2] Laboratory of Molecular Neuroscience, German Center for Neurodegenerative Diseases (DZNE), Berlin 10117, Germany. [3] The Child Health Institute of New Jersey, Robert Wood Johnson Medical School, Rutgers University, New Brunswick, NJ 08901, USA. [4] Department of Neuroscience and Cell Biology, Robert Wood Johnson Medical School, Rutgers University, New Brunswick, NJ 08901, USA. [5] Einstein Center for Neuroscience, Charité-Universitätsmedizin Berlin, Corporate Member of Freie Universität Berlin, Humboldt-Universität Berlin, and Berlin Institute of Health, Berlin 10117, Germany, [6] German Center for Neurodegenerative Diseases (DZNE), Bonn 53127, Germany. [7] Cancer Pharmacology Research Program, Cancer Institute of New Jersey, Rutgers University, New Brunswick, NJ 08901, USA.

e-mails: Z.S.: zheng.shi@rutgers.edu; D.M.: dragomir.milovanovic@dzne.de

Abstract

Synapsin represents a growing list of condensate-forming proteins where the material states of condensates are directly linked to cellular functions (e.g., neurotransmission) and pathology (e.g., neurodegeneration). However, it remains challenging to quantify condensate material properties in living systems. Here, we first identified distinct regulators on the viscosity and interfacial tension of reconstituted synapsin condensates: crowding agent, synaptic vesicles, and the synucleinopathy marker alpha-synuclein. Furthermore, we developed a new approach based on **m**icropipette **a**spiration and whole-cell **pa**tch **c**lamp (MAPAC) that allows material quantifications of synapsin condensates in living cells. Guided by in vitro results, we found the partitioning of alpha-synuclein critically regulates the viscoelasticity of cellular synapsin condensates, a property that varies over 10,000-fold between cells. Overall, our study provides direct quantitative insights into the regulation of synapsin condensates. Importantly, the platform developed in this study can be broadly applied to study the material properties of condensates in living systems.

Introduction

Biomolecular condensates that form through phase separation have recently come to prominence as a key contributor to various cellular functions [1-3]. The viscoelasticity of condensates regulates the kinetics of biochemical reactions in the dense phase, whereas an aberrant increase in condensate viscoelasticity is associated with neurodegenerative diseases [4-10]. Beyond bulk viscoelasticity, there has been a growing interest in the interfacial properties of condensates [11], focusing on their roles in regulating the structure of multiphase condensates [12-16], the growth and size of condensates [17, 18], and the interactions between condensates with other cellular components such as biopolymers [18-20] and membrane-bound organelles [21-25].

Neuronal communication critically relies on the regulated secretion of synaptic vesicles (SVs) at specialized sites termed synapses. The cluster of SVs at the synaptic boutons represents a prominent example of biomolecular condensates [23, 26, 27], assembled by the highly abundant, intrinsically disordered synapsin family of proteins [28, 29]. Synapsin/SV condensates act as reaction centers that are able to recruit alpha-synuclein [30-32], a major synaptic protein implicated in the regulation of SV cycles and pathology of neurodegenerative diseases collectively known as synucleinopathies [33-35]. Genetic data suggest a tight balance of synapsin and alpha-synuclein concentrations that directly affects the mesoscale organization of SV clusters at synapses [36]. The altered concentration of alpha-synuclein disrupts SV packing [37, 38] and impairs neurotransmission [31, 33, 36, 39]. Therefore, the material properties of synapsin condensates and factors that regulate these properties can directly affect neuronal signaling and neurodegenerative diseases.

While previous data provide circumstantial evidence that alpha-synuclein plays a role in the organization of synapsin/SV assemblies, direct measurements are lacking to determine whether and how alpha-synuclein regulates the material state of synapsin condensates due to technical limitations. Recently, we demonstrated that micropipette aspiration (MPA) can be applied to quantify the material properties of condensates [40, 41]. MPA is a label-free technique that directly measures both the viscosity and interfacial tension of condensates [40]. This contrasts with widely used techniques such as fluorescence recovery after photobleaching, single particle tracking, and droplet fusion, where either only the viscosity or a ratio of viscosity to interfacial tension of condensates is probed [42]. However, direct quantifications of condensate material properties in living cells are still challenging.

Here, we first employ MPA to assess reconstituted synapsin condensates and directly demonstrate the advantage of MPA over droplet fusion measurements. We show that removing the N-terminal region of synapsin leads to a reduction in condensate viscosity. In contrast, three factors significantly increase the viscosity of

synapsin condensates: crowding agents (i.e., polyethylene glycol-8000, hereafter named “PEG”), SVs, and alpha-synuclein. However, these factors have distinct effects on the interfacial tension of synapsin condensates: the interfacial tension increases with PEG, decreases with SVs, but remains unaltered with the partitioning of alpha-synuclein. Next, we study the material properties of synapsin condensates in living mammalian cells by developing a correlative **M**P**A** and whole-cell **pa**tch **c**lamp (MAPAC) platform. The recording of cell membrane voltage provides an electrophysiological monitor for cell health [43] and aids in the detection of condensates. In contrast to apparent liquid condensates in vitro, synapsin condensates in cells exhibit significant elasticity. Interestingly, the viscous and elastic moduli of condensates vary by 4 orders of magnitude between cells, and these variations are directly correlated with the partitioning of alpha-synuclein, and, to a lesser extent, the partitioning of synapsin into condensates. Together, our results provide unprecedented quantitative understanding of synapsin condensates, highlighting an effective cellular control of condensate viscoelasticity via compositional modulations. Moreover, we present MAPAC, a broadly applicable platform that allows intricate examinations of individual condensates in living cells.

Results

Synapsin domains and crowding conditions regulate the viscosity and interfacial tension of synapsin condensates.

Synapsin 1 is the most abundant member of the family of synapsin proteins. Full length synapsin 1 (hereafter named “FL synapsin”) comprises an N-terminal membrane binding domain, a central ATP-binding domain, and a C-terminal intrinsically disordered region (IDR) (Figure 1A) [23, 28]. Purified FL synapsin spontaneously forms condensates under physiologically relevant conditions (5 ~ 10 μM synapsin in 150 mM NaCl, 3 ~ 10% PEG, pH 7.4). The phase separation of synapsin is driven by its IDR: deleting IDR abolishes phase separation, while the purified IDR fragment can form condensates on its own [23]. However, it is unclear whether condensates formed by the IDR are distinct, in their material properties, from those consisting of FL synapsin.

Using an optical tweezers-assisted droplet fusion assay (Figure 1B) [40, 42], we found the capillary velocity of IDR condensates (13.0 ± 0.6 μm/s) was more than 10 times faster than that of the FL condensates (0.8 ± 0.1 μm/s; Figure 1C). Notably, reducing the amount of crowding agent (from 10% to 3% PEG) minimally affected the capillary velocity of synapsin condensates (Figure 1B, 1C).

The capillary velocity, which reports a ratio of interfacial tension to viscosity of the studied condensates, does not provide a direct measure of either material property [42]. To address this, we applied MPA to synapsin condensates. All reconstituted synapsin condensates wetted the inner wall of micropipettes (Figure 1D) and the aspiration length (L_p) changed with the square root of time (Figure S1). The responses of reconstituted synapsin condensates were not significantly different from those predicted for purely viscous liquids [41], suggesting condensate elasticities below 5 Pa (Supplementary discussions). By analyzing synapsin condensates under various aspiration pressures (P_{asp}; Figure 1E), we observed linear relations between the aspiration pressure and the effective shear rate (S; Figure 1F). The slope of P_{asp} vs. S reports condensate viscosity (η; Figure 1G) while the intercept reports the interfacial tension of condensates (γ; Figure 1H).

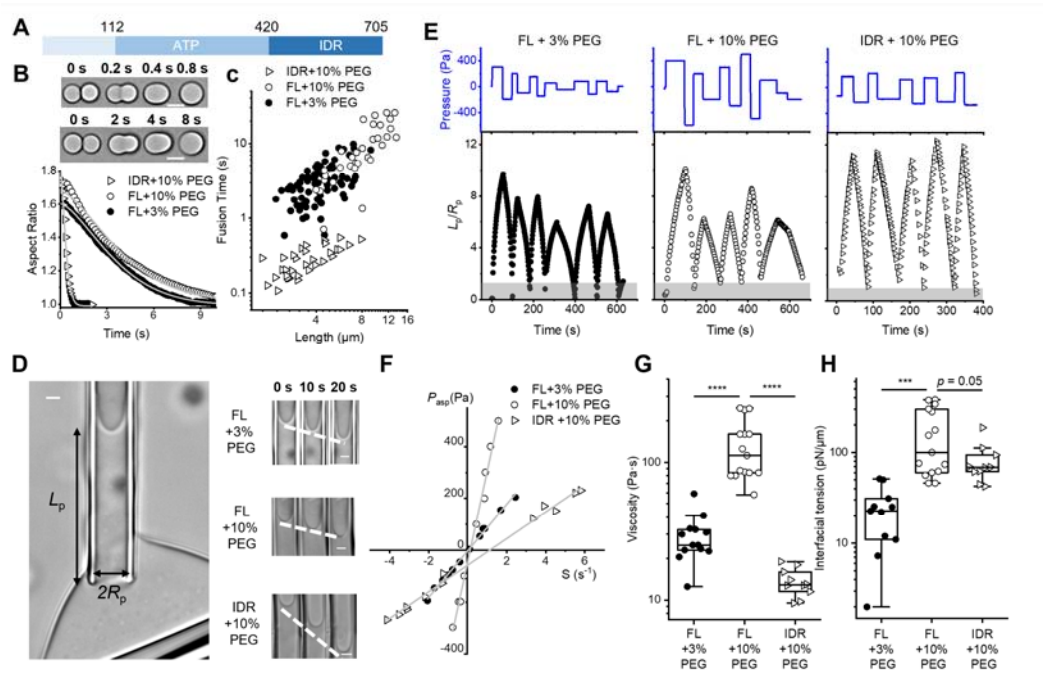

Figure 1: PEG increases both the viscosity and interfacial tension of synapsin condensates while the IDR of synapsin maintains a low condensate viscosity.

(A) Domain diagram of full-length (FL) synapsin 1. **(B)** Images showing the fusion of IDR (upper) and FL (middle) synapsin condensates. Lower: the relaxation of condensate aspect ratios. Grey curves are stretched-exponential fits. Open triangles: IDR under 10% PEG; open circles: FL under 10% PEG; close circles: FL under 3% PEG; same below. Scale bars, 5 μm. **(C)** Condensate fusion time vs. condensate length (the geometric mean of condensate diameters before fusion). The inverse of the slopes from linear fitting gave capillary velocities: 13.0 ± 0.6 μm/s (IDR + 10% PEG; R^2 = 0.93; n = 33 pairs), 0.8 ± 0.1 μm/s (FL + 10% PEG; R^2 = 0.81; n = 34 pairs), and 1.3 ± 0.1 μm/s (FL + 3% PEG; R^2 = 0.82; n = 76 pairs). **(D)** Left: transmitted light image showing a micropipette-aspirated synapsin condensate (held by a

second pipette). Right: time-lapse images showing the flow of FL (upper: + 3% PEG; middle: + 10% PEG) and IDR (lower: + 10% PEG) synapsin condensates under constant aspiration pressure (upper and middle: P_{asp} = -300 Pa; lower: P_{asp} = -250 Pa). $P_{asp} < 0$ corresponds to ejection. All condensates wet the inner wall of micropipettes as indicated by the concave meniscus. Scale bars, 2 μm. **(E)** Aspiration pressure (blue) and normalized aspiration length (black) during MPA of FL (left: +3% PEG; middle: +10% PEG) and IDR (right: +10% PEG) synapsin condensates. The grey shades represent $L_p/R_p < 1$. **(F)** The relationship between aspiration pressure and shear rate S, defined as $S = d(L_p/R_p)^2/dt$, for synapsin condensates. Solid lines are linear fits (all $R^2 > 0.99$). **(G)** Viscosity and **(H)** interfacial tension of FL (+ 3% PEG, n = 13; + 10% PEG, n = 15) and IDR (+ 10% PEG, n= 10) synapsin condensates measured by MPA. All measurements were done with 9 μM synapsin (FL or IDR) in 150 mM NaCl, 25 mM Tris-HCl, 0.5 mM TCEP, pH 7.4. *p* values were determined using one-way ANOVA followed by *post hoc* Tukey's test. ****$p < 10^{-4}$; **$p < 0.01$. In the box plots, the central lines denote the median, the boxes span the interquartile range (25%-75%), and the whiskers extend to 1.5 times the interquartile range, same below.

Under the same crowding condition (10% PEG), the viscosity of IDR condensates (η = 12.9 Pa·s; median, same below) was about 10 times lower than that of FL condensates (112 Pa·s; $p < 10^{-4}$), whereas the interfacial tensions (γ) of the two types of condensates were comparable (p = 0.05). These results are consistent with the ~10-fold faster capillary velocity (γ/η) of IDR than that of FL synapsin condensates (Figure 1C). However, with direct measurements by MPA, we now assign a clear role of the synapsin N-terminal region as a critical mediator of the condensate's viscosity, rather than their interfacial tension, consistent with the N-terminal region's ability to dimerize synapsin [44].

PEG is a commonly used crowding agent that facilitates phase separation of proteins [45, 46]. We observed that reducing the concentration of PEG from 10% to 3% led to significant decreases in both the viscosity (η from 110 to 25 Pa·s; $p < 10^{-4}$, Figure 1G) and interfacial tension (γ from 100 to 23 pN/μm; $p < 10^{-3}$, Figure 1H) of synapsin condensates. However, the capillary velocity (γ/η = 0.89 μm/s in 10% PEG, γ/η = 0.91 μm/s in 3% PEG) of condensates remained largely unaltered. Therefore, only measuring the capillary velocity (i.e., via droplet fusion) would have missed the significant effects of PEG on condensate material properties (for comparison, see Figure 1C). Notably, PEG has been shown to reduce the fluidity of nucleoprotein condensates [45, 46], suggesting a universal crowder-mediated intermolecular attraction in protein condensates [45-48].

Synaptic vesicles increase the viscosity but lower the interfacial tension of synapsin condensates.

A main physiological role of synapsin condensates is to organize the reserve pool of SVs in the presynaptic terminal [23]. Therefore, the material state of synapsin condensates may directly impact SV recycling and neurotransmitter release that are crucial for synaptic transmission. We found that SVs purified from rat brains (visualized with the lipophilic FM 4-64 dye) partition strongly into synapsin condensates (Figure 2A) [26]. Physiological concentrations of SVs (~ 50 nM vesicles [30]) significantly increased the viscosity (p = 0.01) but decreased the interfacial tension (p < 0.01) of synapsin condensates (Figure 2B – 2E, Figure S2A, S2B). The increase in condensate viscosity is consistent with SV's ability to provide multivalent interactions that promote the phase separation of synapsin. With 46 nM SVs, some synapsin/SV condensates became irregularly shaped (Figure S2B), indicating a transition into viscoelastic states for those condensates. The increase of condensate viscosity by SVs suggests that the partitioning of SVs may slow down the transport of vesicles in the reserve pool, consistent with recent single molecular tracking measurements [26]. The reduction in the interfacial tension of condensates by SVs agrees with recent observations that lipid vesicles are prone to perturb the interface of condensates [49], suggesting a role of SVs in mediating the morphological integrity of the reserve pool.

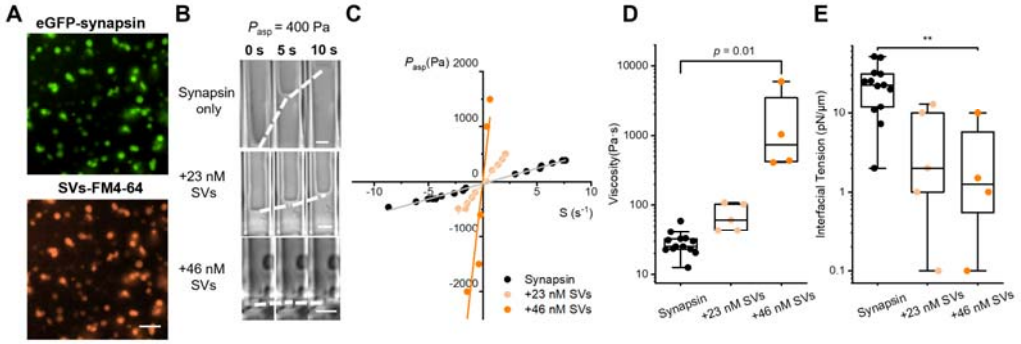

Figure 2: SVs increase the viscosity but lower the interfacial tension of synapsin condensates.

(A) Colocalization of eGFP-synapsin (green) and SVs labeled with FM™ 4-64 (orange). Scale bar, 10 μm. **(B)** Time-lapse transmitted light images showing the deformation of synapsin condensates with increasing concentration of SVs. Dashed lines trace the change in L_p under 400 Pa aspiration pressure. Scale bars, 2 μm. **(C)** Relation between aspiration pressure and shear rate measured on condensates of synapsin only (black), synapsin + 23 nM SVs (light orange), and synapsin + 46 nM SVs (orange). Effect of SV on the viscosity **(D)** and interfacial tension **(E)** of synapsin condensates. All measurements were done with 9 μM synapsin FL in 3% PEG, 150 mM NaCl, 25 mM Tris-HCl, 0.5 mM TCEP, pH 7.4. p values were determined using one-way ANOVA followed by *post hoc* Tukey's test. $^{**}p < 0.01$.

Alpha-synuclein increases the viscosity of synapsin condensates in a self-catalytic manner.

Beyond organizing SV clusters, synapsin condensates recruit a range of client proteins [50]. A prominent member of these clients is alpha-synuclein, known for its involvement in Parkinson's disease and other synucleinopathies [30]. The partitioning of alpha-synuclein did not affect the wetting of synapsin condensates to micropipettes (Figure 3a, 3B), and synapsin/alpha-synuclein condensates remained purely viscous liquids within the timescale of our MPA measurements (Figure 3C, Figure S2C, S2D). However, the viscosity of condensates significantly increased in the presence of alpha-synuclein ($p < 10^{-3}$; Figure 3D), whereas the interfacial tension of synapsin condensates was not significantly perturbed ($p = 0.06$; Figure 3E). The increase in condensate viscosity suggests that alpha-synuclein reduces the dynamics of intermolecular contact within the condensate phase [7], consistent with the observed attenuation of SV recycling in neurons that overexpress alpha-synuclein [31, 39, 51]. Notably, this effect was nonlinear: 3 μM alpha-synuclein caused minimal viscosity increase ($p = 0.13$), while a ~50-fold increase in condensate viscosity was observed in the presence of 9 μM alpha-synuclein (Figure 3D).

Under low concentrations of alpha-synuclein, the protein's affinity towards synapsin condensates can be evaluated via its condensate partitioning coefficient ($\Pi_{\alpha\mathrm{Syn}}$; i.e., the concentration of alpha-synuclein in condensates relative to that in the dilute phase; Supplementary discussions). $\Pi_{\alpha\mathrm{Syn}}$, albeit larger than 1, was much lower than the condensate partitioning coefficient of synapsin (Π_{synapsin}) (Figure 3f, Figure S3), reminiscent to the observation of alpha-synuclein being a client protein recruited to condensates formed by synapsin [30]. However, $\Pi_{\alpha\mathrm{Syn}}$ increased with alpha-synuclein concentration (Figure 3F), suggesting a homotropic cooperativity between alpha-synuclein molecules in their partitioning to synapsin condensates. Meanwhile, Π_{synapsin} remained constant with increasing amount of alpha-synuclein (Figure S3D). This cooperativity between alpha-synuclein is in line with the protein's nonlinear effect on the viscosity of synapsin condensates (Figure 3D).

The size distribution of condensates represents a balance between condensate interfacial tension and the mixing entropy of the system [14]. The size of synapsin/alpha-synuclein condensates remained constant under a wide range of alpha-synuclein concentrations (Figure 3G), in agreement with the lack of alpha-synuclein effect on the interfacial tension of synapsin condensates (Figure 3E).

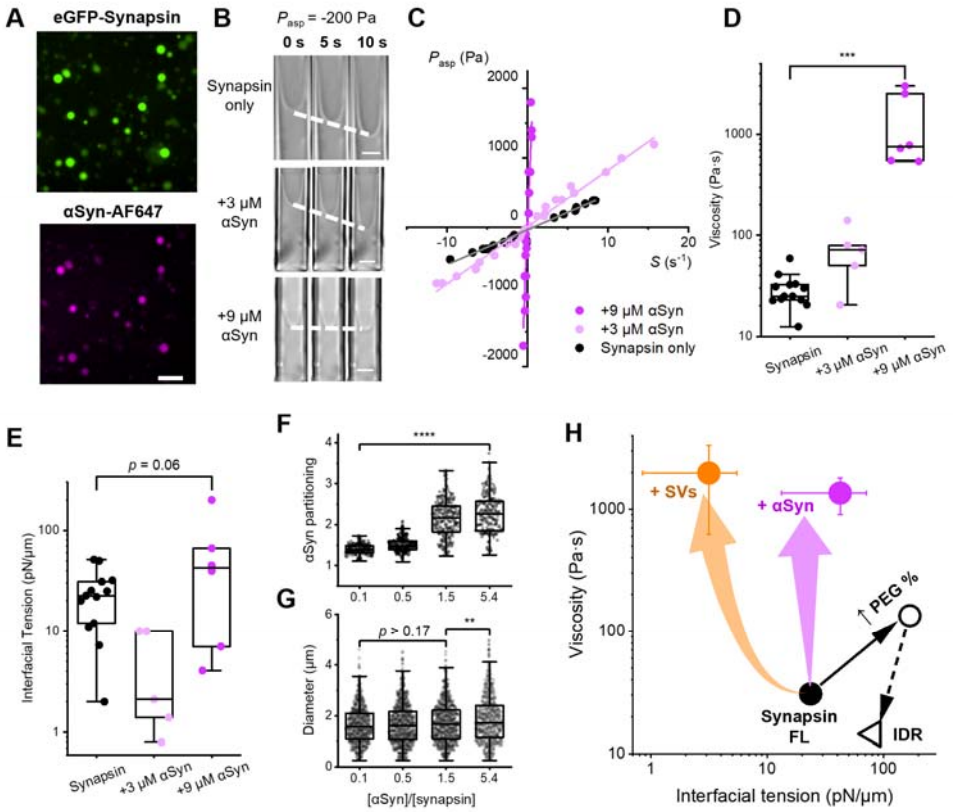

Figure 3: alpha-synuclein increases the viscosity but does not significantly perturb the interfacial tension of synapsin condensates.

(A) Colocalization of eGFP-synapsin (green) and alpha-synuclein (magenta; wild type alpha-synuclein mixed with Alexa Fluor 647 labelled alpha-synuclein-A140C in a 10:1 ratio). Scale bar: 10 μm. **(B)** Time-lapse transmitted light images of synapsin condensate with increasing concentration of alpha-synuclein. Dashed lines trace the change in L_p under -200 Pa aspiration pressure. Scale bars: 2 μm. **(C)** Relation between aspiration pressure and shear rate measured on condensates of synapsin only (black), synapsin + 3 μM alpha-synuclein (light magenta), and synapsin + 9 μM alpha-synuclein (magenta). The solid lines are linear fits. Effect of alpha-synuclein on the viscosity **(D)** and interfacial tension **(E)** of synapsin condensates. **(F)** The partitioning of alpha-synuclein to synapsin condensates with increasing molar ratio of alpha-synuclein to synapsin. **(G)** The diameter of synapsin condensates with increasing molar ratio of alpha-synuclein to synapsin. **(H)** Viscosity and interfacial tension of in vitro synapsin condensates. Closed circles represent FL only (black), FL + 9 μM alpha-synuclein (magenta), or FL + 46 nM SVs (orange) in 3% PEG. Open markers represent FL (circle) and IDR (triangle) in 10% PEG. Error bars are SEM. Synapsin concentration was 9 μM in **(A)−(E),** 5 μM in **(F)** and **(G).** Buffer: 150 mM NaCl, 25 mM Tris-HCl, 0.5 mM TCEP, pH 7.4. *p* values were determined using one-way ANOVA followed by *post hoc* Tukey's test. $^{**}p < 0.01$; $^{***}p < 10^{-3}$; $^{****}p < 10^{-4}$.

Taken together, our in vitro study suggests that the liquidity of synapsin condensates can be fully controlled via biologically relevant factors. The presence of alpha-synuclein, SV, and PEG (mimicking the crowding condition of the cytoplasm) all render synapsin condensates more viscous, while removing the N-terminal region of synapsin reduces condensate viscosity (Figure 3H). Viscosity is a kinetic parameter that is governed by the dynamics of molecular interactions within the condensate [7], whereas interfacial tension is a thermodynamic parameter that depends on both the dense and the dilute phases [11]. Indeed, we found that the interfacial tension and viscosity of condensates can be independently tuned: PEG increases, whereas SVs decrease the interfacial tension of synapsin condensates (Figure 3H). Notably, measurements on condensates formed by a ternary mixture of synapsin/SV/alpha-synuclein suggested weak competitions between the effects of alpha-synuclein and SV on synapsin condensates (Figure S4).

The effect of alpha-synuclein on the viscosity of synapsin condensates is particularly interesting due to its relevance to the dynamics of synaptic vesicle release [39, 51] and to neurodegenerative diseases (e.g., Parkinson's) that are marked by alpha-synuclein containing solid aggregates [52-55]. However, condensate properties and conditions that regulate them in vitro may not faithfully represent those in living systems. To further elucidate condensate properties in a cellular context, we developed a new approach, MAPAC (**M**P**A** and whole-cell **pa**tch **c**lamp), to achieve direct measurements of condensate material properties in live cells.

MAPAC allows direct measurements of synapsin condensates in live cells.

To probe condensates in live cells, an electrode-containing micropipette filled with intracellular buffer solution was positioned to break the plasma membrane near a condensate (Figure 4A). Once the plasma membrane sealed to the pipette tip, suction pressures were gently applied so that the nearby condensate could flow into the tip of the micropipette for subsequent quantifications. Meanwhile, the recorded membrane voltage served as a sensitive monitor for the integrity of the membrane seal and the stability of the intracellular environment during MAPAC.

First, we tested the effect of aspiration pressure on the stability of voltage recording. Under frequent pressure perturbations that resemble those used to probe condensate material properties, the measured membrane voltage on HEK 293T cells was stable for tens of minutes until purposefully perturbed by an ejection pressure that broke the membrane seal (Figure S5A). A similar time window was maintained in cells over-expressing synapsin and alpha-synuclein (Figure 4B), sufficient for

extensive aspiration measurements where each pressure step takes ~ 10 seconds. In addition to membrane voltage, the fluorescence of cytosolic proteins can be used as a secondary monitor for potential leakages at the cell membrane (Figure 4B).

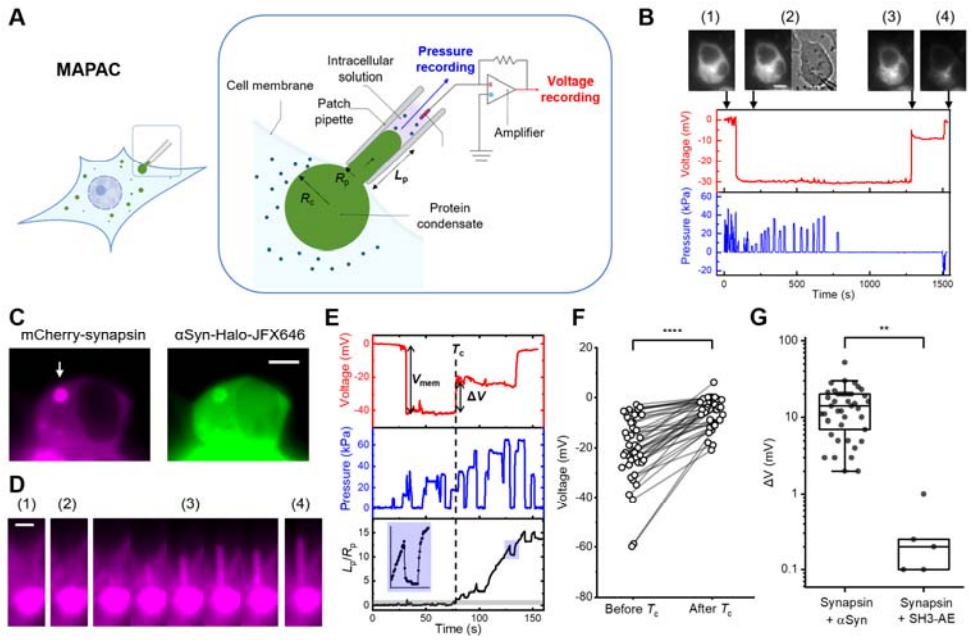

Figure 4: Development of MAPAC for condensate measurements in live cells.

(A) Schematic representation of the MAPAC platform. The subcellular region where the micropipette broke into the cell and aspirated a condensate is zoomed-in on the right. **(B)** An example testing the effect of aspiration pressure (blue) on cell membrane voltage recording (red) on a HEK 293T cell expressing mCherry-synapsin and alpha-synuclein-BFP. Four fluorescence images of synapsin correspond to timepoints before (1) and after (2) break-in; before (3) and after (4) losing membrane seal. A transmitted light image is included for timepoint (2) to show the patched cell and the position of the micropipette. The voltage signal before timepoint (3) corresponded to a motion of the micropipette tip that either contacted the condensate or weakened the membrane seal. The voltage jumped to 0 mV before timepoint (4) due to an intentional ejection pressure that broke the membrane seal. Significant leakage of cytosolic fluorescence was observed after the ejection pressure. **(C)** Fluorescence images showing a HEK 293T cell co-expressing mCherry-synapsin (magenta) and alpha-synuclein-Halo (stained with JFX-646; green). The arrow represents the micropipette that was positioned next to a condensate. **(D)** Fluorescence images of the synapsin/alpha-synuclein condensate before (1) and after (2) micropipette break-in, during MAPAC (3), and after V_{mem} jumped to zero (4). **(E)** MAPAC recording of membrane voltage (red), aspiration pressure (blue), and aspiration length (black; normalized to pipette radius) for the condensate in **(D)**. The entrance of the condensate into pipette tip at T_c (dashed line) accompanied a voltage jump (ΔV). The grey shade on L_p/R_p represents $L_p/R_p < 1$. The blue shade on L_p/R_p is

zoomed-in on the left, showing viscoelastic responses of the condensate to pressure steps. **(F)** Voltage recordings before and after a synapsin/alpha-synuclein condensate entered the tip of the micropipette. n = 41 cells. **** $p < 10^{-4}$, paired t test. **(G)** ΔV measured on synapsin/alpha-synuclein condensates and synapsin/intersectin-SH3 condensates (n = 5). ** $p < 10^{-2}$, Student's t test. All scale bars are 5 µm, except 2 µm in **(D)**.

In HEK 293T cells, the expression of synapsin alone was not sufficient to drive condensate formation, likely due to the lack of other neuronal components naturally occurring to promote phase separation at the nerve terminal. Indeed, co-expressing synapsin with alpha-synuclein or intersectin SH3 domains robustly induced micrometer-size synapsin condensates (Figure 4C, Figure S5) [30]. We focused our further study on a minimal system with HEK 293T cells co-expressing fluorescently tagged synapsin and alpha-synuclein (Figure 4C). These cells typically have one (occasionally two) major condensate with a radius R_c = 1.5 ± 0.6 µm (mean ± SD, n = 74; Figure S5B), sufficient for accurate aspiration measurements with narrow micropipettes (opening diameter ~1 µm; Figure 4D; Movie S1).

After breaking into the cell but before aspirating a condensate, the electrode-containing micropipette measures the resting voltage of the cell membrane (V_{mem}; Figure 4E). On non-transfected cells, the recorded V_{mem} = -49 ± 6 mV (mean ± SEM, n = 7; Figure S5C) was consistent with membrane potentials reported for healthy HEK 293T [56]. Cells expressing synapsin and alpha-synuclein showed a less polarized membrane potential (V_{mem} = -23 ± 2 mV; mean ± SEM, n = 47; $p < 0.01$; Figure S5C), indicating an electrophysiological perturbation by the expressed neuronal proteins. Interestingly, a voltage jump (ΔV) was observed when synapsin/alpha-synuclein condensates entered the tip of the micropipette (Figure 4E). The measured ΔV = 15 ± 1.5 mV (mean ± SEM, n = 41; $p < 10^{-4}$; Figure 4F) might suggest that synapsin/alpha-synuclein condensates have significantly increased the resistance to ion flow into the micropipette [57, 58]. Interestingly, ΔV was more significant for synapsin condensates driven by alpha-synuclein than those driven by intersectin SH3 domains (Figure 4G; $p < 0.01$), which might indicate different porosity [59], thus electrical resistance, of these condensates. On a technical note, ΔV can be used to aid label-free detections of condensates by the micropipette tip.

Synapsin condensates in cells are viscoelastic.

After a condensate entered the tip of the micropipette, controlled pressure steps were applied to examine the material properties of the condensate (Figure 4E; Movie S1). Unlike in vitro synapsin condensates which appeared purely viscous under MPA (Figure 1 – Figure 3), most synapsin condensates in cells showed clear features of

viscoelasticity, as indicated by sudden nonlinear jumps of L_p upon stepwise pressure changes (Figure 4e, Figure S5D – S5F). Additionally, cellular condensates did not wet the inner wall of micropipettes: condensates inside the micropipette formed a convex meniscus, could undergo necking instability, and did not leave behind any measurable fluorescence after leaving the micropipette (Figure S6). Consistent with a slipping contact between the condensate and the micropipette, the long-term response of L_p under constant pressure appeared linear (Figure 4E, 5A) [41, 60].

Across ~ 100 synapsin/alpha-synuclein condensates in HEK 293T cells, we observed material responses ranging from apparent viscous liquid (Figure 5A, black) to viscoelastic liquid (Figure 5A, red) and to apparent elastic solid (Figure 5A, blue). We found that a 3-element viscoelastic liquid (Jeffreys) model is minimally required to explain all condensate responses observed in cells (Figure 5B; Supplementary discussions) [61]. The model includes a viscous liquid component (η_1) that governs the long-term condensate response, in series with a viscoelastic solid component (E and η_2) that determines the short-term response (Figure 5B) [60]. Under constant pressure, the time-dependent aspiration length (L_p, normalized to the micropipette radius R_p) follows equation (1):

$$\frac{L_\mathrm{p}}{R_\mathrm{p}} = \left(\frac{L_\mathrm{p}}{R_\mathrm{p}}\right)_0 + A\left[1 - e^{-\frac{(t-t_0)}{\tau}}\right] + B(t - t_0) \qquad (1)$$

$\left(\frac{L_\mathrm{p}}{R_\mathrm{p}}\right)_0$ is the normalized aspiration length before a stepwise pressure change at time t_0. The model has three fitting parameters: $A = \frac{P}{E}$, $B = \frac{P}{\eta_1}$, and $\tau = \frac{\eta_2}{E}$. Here, $P = P_\mathrm{asp} - P_\gamma$, and $P_\gamma = 2\gamma\left(\frac{1}{R_\mathrm{p}} - \frac{1}{R_\mathrm{c}}\right)$ is the capillary pressure that needs to be overcome to initiate condensate flow. In this model, an apparent elastic condensate (Figure 5A, blue) will have an infinite viscosity, whereas an apparent viscous condensate (Figure 5A, black) can have zero elasticity. We assigned these extreme cases using the resolution of our experiments (Supplementary discussions).

Next, we measured the "L_p/R_p" of condensates under systematically varied steps of P_{asp} (Figure 5C; Movie S2). The slopes of "P_{asp} vs. B" and "P_{asp} vs. A" give η_1 and E, respectively, whereas the intercepts give P_γ (Figure 5D, 5E). η_1, E, and P_γ can then be converted to the viscosity, elasticity, and interfacial tension of the measured condensate, respectively (Supplementary discussions) [60, 62].

Notably, a 2-parameter linear model can be applied to the long-term response of L_p (Figure 5B, 5C) [60]. The resulting "P_{asp} vs. B" and "P_{asp} vs. A" relations were indistinguishable from those of the full 3-parameter model (Figure 5D, 5E, Figure S7).

By sacrificing the fitting for η_2 (Figure S7F), a property not directly related to the material state of the condensate [61], the linear model reduced fitting errors, especially for data with low signal to noise ratio and for data where the pressure profile significantly deviated from a step-function (Figure S7). Therefore, we used the linear model for all further analysis of cellular condensates.

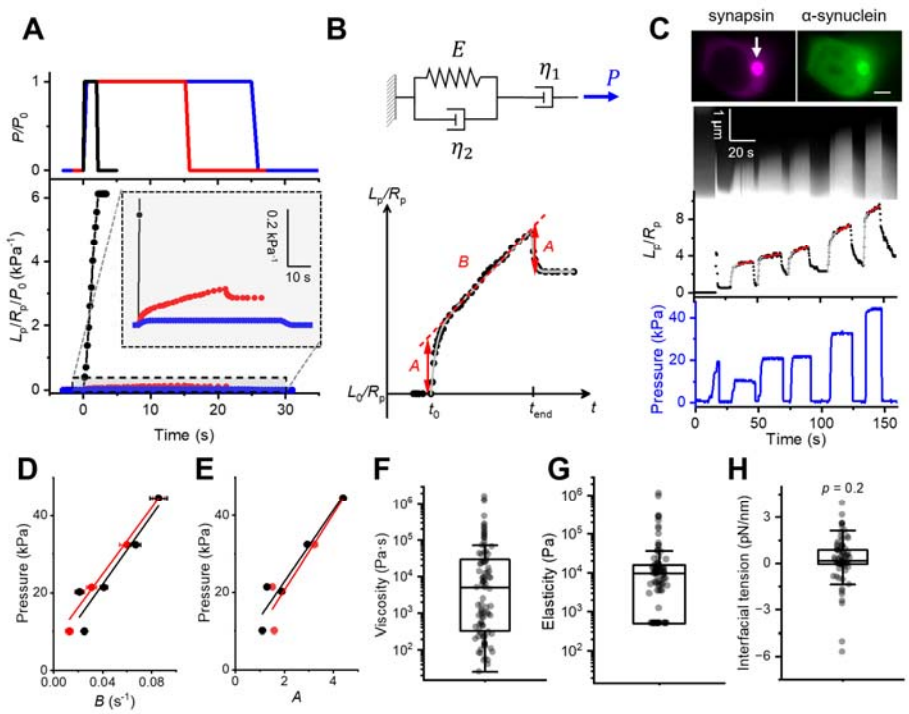

Figure 5: Cellular synapsin condensates quantified by a 3-element viscoelastic liquid model.

(A) Representative responses of cellular synapsin/alpha-synuclein condensates to a stepwise aspiration pressure. Black: apparent viscous liquid, 24/93 condensates; red: viscoelastic liquid, 53/93 condensates; blue: apparent elastic solid, 16/93 condensates. The boxed area is zoomed-in to improve the display of the red and blue data. **(B)** Upper: the 3-element viscoelastic liquid model used for analyzing all cellular condensates. Lower: fitting of a representative condensate response to the full model (3-parameter; grey) or to a simplified linear model (2-parameter, red). *S* is the long-term shear rate; *A* is the normalized amplitude of the elastic response. **(C)** Upper: fluorescence images of a HEK 293T cell co-expressing mCherry-synapsin (magenta) and alpha-synuclein-Halo labeled with JFX-646 (green), arrow points to the condensate, scale bar 5 µm. Middle: kymograph of the aspirated part of the condensates. Lower: normalized aspiration length (black), in response to stepwise aspiration pressure (blue). Grey curves are fits to the full model (eq. 1); red lines are linear fits. **(D-E)** Aspiration pressures (P_{asp}) plotted against either the long-term shear rate *B* (**D)** or the normalized amplitude of elastic response *A* (**E**). Black and red markers represent results from

the full model and linear model, respectively. Lines are linear fits. **(F-H)** Material properties of synapsin condensates in cells. Viscosity (**F)** was calculated from the slope of **d** (n = 93); elasticity (**G)** was calculated from the slope of **e** (n = 93), 24 condensates with apparent pure viscous response were assigned an elasticity of 500 Pa that corresponded to the experimental resolution; interfacial tension (**H)** was calculated from the intercepts of **D** and **E** (n = 77). *p* value from one sample t-test.

Cellular synapsin condensates exhibited viscoelastic moduli that span over 4 orders of magnitude (Figure 5F, 5G; n = 93) from liquid states that resemble in vitro synapsin condensates (viscosity < 100 Pa·s; negligible elasticity) to apparent solid states that cannot be measurably deformed (viscosity ~ 10^6 Pa·s; elasticity ~ 10^6 Pa). The viscoelasticity of cellular condensates represents intrinsic properties of the condensate-forming proteins, as they did not depend on the resting potential of the cell and was not significantly affected by the choice of fluorescent tags (Figure S8).

The measured interfacial tension of cellular condensates (γ = 240 ± 220 pN/μm; mean ± SEM, n = 77; Figure 5H, Figure S9) was not significantly different from zero (p = 0.2), consistent with the low interfacial tension of synapsin/alpha-synuclein condensates in vitro (~30 pN/μm; Figure 3E). The uncertainties in interfacial tension correspond to a capillary pressure P_γ (~ 1 kPa) that does not significantly affect aspiration pressures used for viscoelasticity measurements (10 ~ 50 kPa; Figure 5C).

The median viscosity of cellular condensates (5000 Pa·s; Figure 5F) was 200 times higher than that of pure synapsin condensates in vitro (25 Pa·s; Figure 1G) but comparable to synapsin/alpha-synuclein condensates reconstituted with 9 μM of synapsin and 9 μM of alpha-synuclein (~1000 Pa·s; Figure 3D). Therefore, we next explored whether the partitioning of alpha-synuclein played a role in determining the viscoelasticity of synapsin condensates in cells.

Condensate partitioning of alpha-synuclein and synapsin dictate the viscoelasticity of synapsin condensates in cells.

When alpha-synuclein and synapsin were heterogeneously expressed in HEK 293T cells, $\Pi_{\alpha\mathrm{Syn}}$ spanned two orders of magnitude, from weakly depleted from condensates ($\Pi_{\alpha\mathrm{Syn}}$ < 1) to highly enriched in the condensate phase ($\Pi_{\alpha\mathrm{Syn}}$ > 10; Figure S10A – S10C). In comparison, Π_{synapsin} was more clustered (~ 10) and overall higher than $\Pi_{\alpha\mathrm{Syn}}$ (p < 10^{-4}), consistent with our observations in vitro (Figure 3F, S3D).

For synapsin/alpha-synuclein condensates with comparable Π_{synapsin} (10 ± 3), we found $\Pi_{\alpha\mathrm{Syn}}$ to be an accurate prophecy of the condensate's viscoelastic response under MAPAC: condensates with $\Pi_{\alpha\mathrm{Syn}}$ ~ 1 easily flowed under pressure; the flow of

~ 5 condensates was ~100 times slower; whereas condensates with > 10 were barely deformable (Figure 6A).

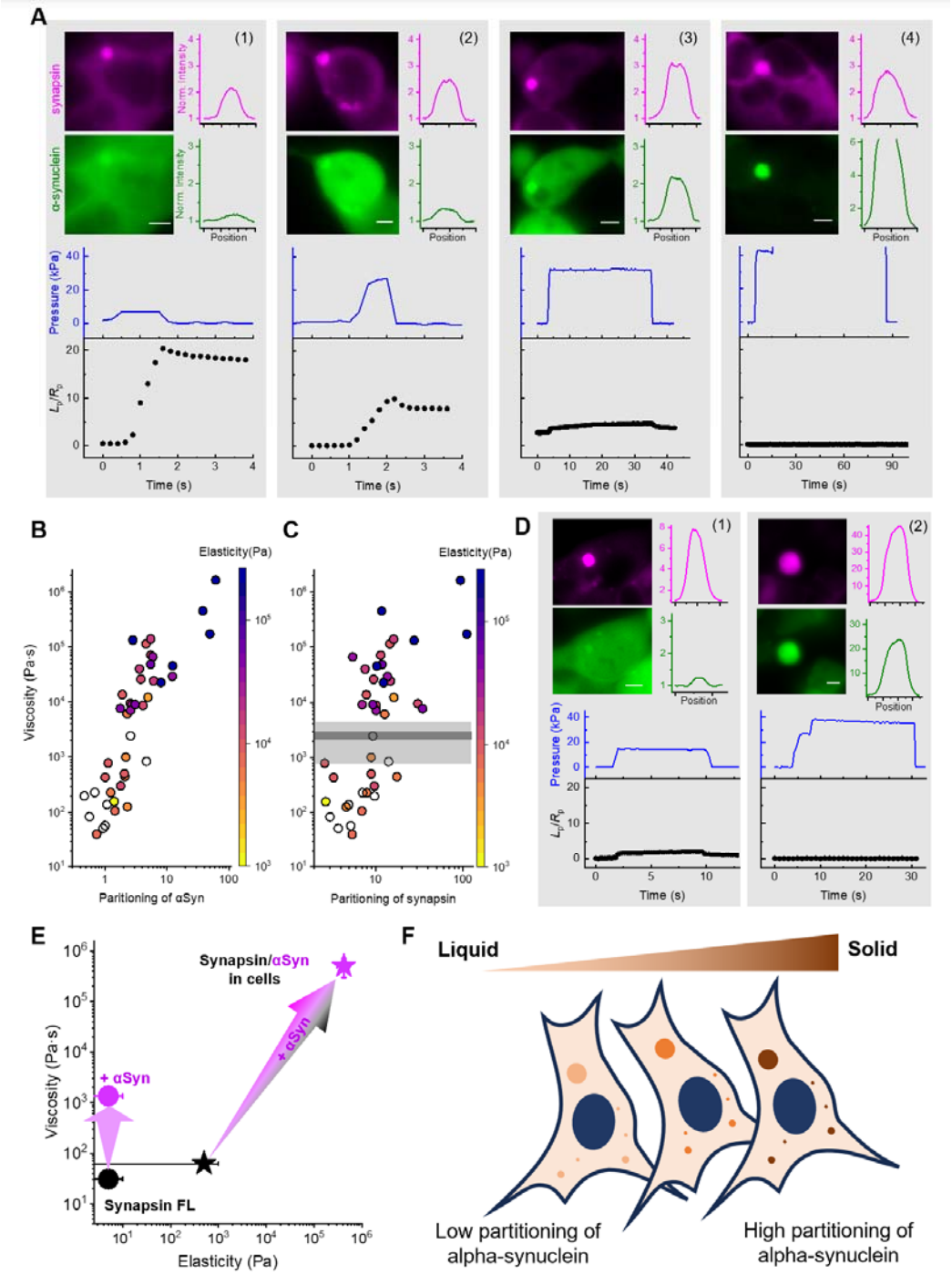

Figure 6: The partitioning of alpha-synuclein dictates the viscoelasticity of synapsin condensate in cells.

(A) Upper: widefield fluorescence images of four HEK 293T cells co-expressing mCherry-synapsin (magenta) and alpha-synuclein-Halo labelled with JFX-646 (green), with fluorescence intensity profiles across the condensate plotted on the right of each image. These four condensates have similar partitioning of synapsin but drastically different partitioning of alpha-synuclein, from (1) to (4): Π_{synapsin} = 5.2, 9.7, 13.7, 11.7; and $\Pi_{\alpha\mathrm{Syn}}$ = 1.0, 1.8, 5.5, 38, respectively. See Figure S10 for conversion from apparent partitioning measured from widefield to true partitioning measured from confocal microscopy. Lower: applied aspiration pressure step (blue) and corresponding response of each condensate (black). All graphs have the same scale in P_{asp} and $L_{\mathrm{p}}/R_{\mathrm{p}}$. The condensate increased in viscosity and elasticity from (1) to (4). **(B, C)** The relationships between the viscosity of 43 condensates as a function of $\Pi_{\alpha\mathrm{Syn}}$ (**B)** or Π_{synapsin} (**C)**. The elasticity of each condensate was colored according to the map. White condensates did not show measurable elastic response and was assigned an elasticity of 500 Pa. The gray line and shade represent the mean and standard deviation of the system viscosity (η_2/6) measured from the full model. **(D)** Upper: widefield fluorescence images of two HEK 293T cells co-expressing mCherry-synapsin (magenta) and alpha-synuclein-Halo labelled with JFX-646 (green), with fluorescence intensity profiles across the condensate plotted on the right of each image. From (1) to (2): Π_{synapsin} = 35, 93; and $\Pi_{\alpha\mathrm{Syn}}$ = 1.8, 61, respectively. Lower: applied aspiration pressure step (blue) and corresponding response of each condensate (black). **(E)** Viscosity and elasticity of synapsin condensates. Circles represent in vitro condensates (black: FL synapsin only; magenta: FL synapsin + 9 μM alpha-synuclein) and were assigned an elasticity of 5 Pa. Stars represent synapsin/alpha-synuclein condensates in cells with low (black) and high (magenta) partitioning of alpha-synuclein. Error bars are SEM. **(F)** An illustration showing that the partitioning of alpha-synuclein dictates the material state of synapsin condensates in cells. All scale bars are 5 μm.

Across 43 cells that co-expressed mCherry-synapsin 1 and alpha-synuclein-Halo (stained with JFX-646), the viscoelasticity of formed condensates was strongly correlated with $\Pi_{\alpha\mathrm{Syn}}$ (Figure 6B, Figure S10D; Pearson's r = 0.84 for viscosity, r = 0.74 for elasticity). In contrast, the viscoelasticity was not dependent on the apparent concentrations of alpha-synuclein in the cytosol (r = 0.08; Figure S10E) and was only weakly dependent on the apparent concentration of alpha-synuclein in the condensate (r = 0.39; Figure S10F), consistent with the partitioning coefficient being a better indicator of alpha-synuclein's affinity towards the condensates (Supplementary discussions). Additionally, the measured viscoelasticity and partitioning coefficients were independent of condensate radius (r = 0.14; Figure S10G), confirming the lack of optical artifacts induced by condensate curvature [63]. The interfacial tension of cellular condensates did not show significant dependence on the partitioning of either alpha-synuclein or synapsin (Figure S9), consistent with our observations in vitro (Figure 3E).

Unlike in vitro conditions (Figure 3F, S3D), a positive correlation (r = 0.68) was observed between $\Pi_{\alpha\mathrm{Syn}}$ and Π_{synapsin} in cells (Figure S10H), indicating the presence

of cellular factors that promoted heterotropic cooperativity between alpha-synuclein and synapsin. Consequently, Π_{synapsin} can also predict the viscoelasticity of cellular condensates (Figure 6C, Figure S10I – S10K; r = 0.66 for viscosity, r = 0.60 for elasticity) albeit less accurately compared to $\Pi_{\alpha\mathrm{Syn}}$. Condensates with $\Pi_{\alpha\mathrm{Syn}}$ ~ 1 but Π_{synapsin} > 30 showed strong viscoelastic features, while condensates with high values (> 30) of both $\Pi_{\alpha\mathrm{Syn}}$ and Π_{synapsin} were not measurably deformable (Figure 6D). Linear combinations of $\Pi_{\alpha\mathrm{Syn}}$ and Π_{synapsin} did not outperform $\Pi_{\alpha\mathrm{Syn}}$ alone in predicting the viscoelasticity of cellular condensates (Figure S10l), consistent with the partition of alpha-synuclein being the main driver for the viscoelasticity of synapsin condensates in cells.

Discussion

Our in vitro results highlight multiple distinct pathways that can regulate the viscosity and interfacial tension of synapsin condensates (Figure 3H). Factors that promote the phase separation of synapsin condensates (e.g., PEG, SVs, and alpha-synuclein) generally increase condensate viscosity. However, these factors can have distinct effects on the interfacial tension of condensates, highlighting the complexity of condensate interfaces [64].

MAPAC allowed us to carry out the first quantitative study of the material properties of condensates in living cells. Compared to synapsin condensates in vitro, cellular condensates were significantly more elastic (Figure 6E). The upper limit for the elasticity of in vitro synapsin condensate (5 Pa) was three orders of magnitude lower than the median elasticity of cellular synapsin condensates (10 kPa). Therefore, characterizations in live cells are crucially needed to understand the material properties of condensates in their natural environment. The viscoelasticity of cellular synapsin condensates spanned over four orders of magnitude. Guided by in vitro characterizations (Figure 3), we were able to identify the partitioning of alpha-synuclein as a key regulator of the viscoelasticity of cellular synapsin condensates (Figure 6). Our results highlight the importance of coordinated live cell and in vitro measurements in deconstructing the determinants of the material properties of biological condensates.

Our measurements of cellular synapsin condensates also show that the morphology of condensates (such as sphericity [65]) carries little information about their material properties. Although the majority of synapsin condensates were spherical, their viscoelasticity varied drastically, from low-viscosity liquid that allows dynamic molecular exchange to apparent solid that resembles disease-associated inclusions such as Lewy bodies [52-54] (Figure 6). Unlike condensate morphology, the partitioning of key regulatory proteins (i.e., alpha-synuclein) can be an accurate predictor of

condensate material properties (Figure 6F). Posttranslational modifications such as phosphorylation may provide an additional layer of viscoelastic regulation. This is particularly relevant in the case of synaptic activity, where upon activation a global series of phosphorylation events targets numerous proteins [66], including synapsin 1 and alpha-synuclein [67, 68]. These phosphorylation events may affect the clustering of synaptic vesicles in vertebrate synapses [37, 68, 69], further emphasizing the importance of direct in vivo quantification of viscoelasticity. To fully understand synapsin biology, future efforts will focus on exploring the roles of synaptic vesicles, disease related mutations, and posttranslational modifications in modulating the material properties of synapsin condensates under physiological conditions.

The interfacial tension of synapsin/alpha-synuclein condensates in cells showed large measurement uncertainties (Figure 5H, S9). This is likely due to the low resolution of the pressure system used for cellular measurements (resolution ~100 Pa in cell vs. ~1 Pa in vitro). The compromise in resolution is needed to reach sufficiently large P_{asp} to break into the cell and to deform the highly viscoelastic condensates (Methods). As a result, we observed no statistical difference between the interfacial tension of synapsin/alpha-synuclein condensates in vitro and in cells (Figure 3E, Figure S9). However, the ~10-fold higher mean value of the interfacial tension of cellular condensates may reflect biomolecular assemblies (e.g., cytoskeleton) at the condensate interface that resisted the initial condensate deformation under MPA [70]. Alternatively, the high interfacial tension of cellular synapsin condensates may indicate that the intracellular environment was more crowded than the 3% PEG condition used for in vitro studies (Figure 1H).

MAPAC shares a large part of its hardware with patch-clamp, a well-established tool in electrophysiology, making it easily accessible to neuroscience, biophysics, and cell biology communities [43]. The typical opening diameter of micropipettes used in MAPAC is 0.5 ~ 1 μm, best suited for studying cytosolic condensates with a diameter >1.5 μm. Micrometer-sized condensates are widely observed in the literature, from p granules, stress granules, to those formed by proteins that represent hallmarks of neurodegeneration [4, 5, 8]. Moreover, the electrical recording capacity of MAPAC opens the door to scrutinizing the coupling between electrical, mechanical, and chemical properties of condensates in live cells [57, 58]. Understanding the electrical signals associated with synapsin/alpha-synuclein condensates (Figure 4) will be a steppingstone towards these directions. Therefore, we expect MAPAC to be a broadly accessible and powerful tool for quantitatively understanding biomolecular condensates in living organisms.

References

1. Shin, Y. & Brangwynne, C. P. Liquid phase condensation in cell physiology and disease. *Science* **357** (2017).

2. Banani, S. F., Lee, H. O., Hyman, A. A. & Rosen, M. K. Biomolecular condensates: organizers of cellular biochemistry. *Nature reviews Molecular cell biology* **18**, 285-298 (2017).

3. Su, Q., Mehta, S. & Zhang, J. Liquid-liquid phase separation: Orchestrating cell signaling through time and space. *Mol. Cell* **81**, 4137-4146 (2021).

4. Alberti, S. & Dormann, D. Liquid–liquid phase separation in disease. *Annu. Rev. Genet.* **53**, 171-194 (2019).

5. Mathieu, C., Pappu, R. V. & Taylor, J. P. Beyond aggregation: Pathological phase transitions in neurodegenerative disease. *Science* **370**, 56-60 (2020).

6. Jawerth, L. *et al*. Protein condensates as aging Maxwell fluids. *Science* **370**, 1317-1323 (2020).

7. Sundaravadivelu Devarajan, D. *et al*. Sequence-dependent material properties of biomolecular condensates and their relation to dilute phase conformations. *Nature Communications* **15**, 1912 (2024).

8. Zbinden, A., Pérez-Berlanga, M., De Rossi, P. & Polymenidou, M. Phase separation and neurodegenerative diseases: a disturbance in the force. *Developmental cell* **55**, 45-68 (2020).

9. Rhine, K. *et al*. ALS/FTLD-linked mutations in FUS glycine residues cause accelerated gelation and reduced interactions with wild-type FUS. *Mol. Cell* **80**, 666-681. e8 (2020).

10. Peskett, T. R. *et al*. A liquid to solid phase transition underlying pathological huntingtin exon1 aggregation. *Mol. Cell* **70**, 588-601. e6 (2018).

11. Gouveia, B. *et al*. Capillary forces generated by biomolecular condensates. *Nature* **609**, 255-264 (2022).

12. Fisher, R. S. & Elbaum-Garfinkle, S. Tunable multiphase dynamics of arginine and lysine liquid condensates. *Nature communications* **11**, 4628 (2020).

13. Zwicker, D. & Laan, L. Evolved interactions stabilize many coexisting phases in multicomponent liquids. *Proceedings of the National Academy of Sciences* **119**, e2201250119 (2022).

14. Rana, U. *et al*. Asymmetric oligomerization state and sequence patterning can tune multiphase condensate miscibility. *Nature Chemistry*, 1-10 (2024).

15. Choi, S., Meyer, M. O., Bevilacqua, P. C. & Keating, C. D. Phase-specific RNA accumulation and duplex thermodynamics in multiphase coacervate models for membraneless organelles. *Nature Chemistry* **14**, 1110-1117 (2022).

16. Feric, M. *et al*. Coexisting liquid phases underlie nucleolar subcompartments. *Cell* **165**, 1686-1697 (2016).

17. Cochard, A. *et al*. RNA at the surface of phase-separated condensates impacts their size and number. *Biophys. J.* **121**, 1675-1690 (2022).

18. Banerjee, D. S. *et al*. Interplay of condensate material properties and chromatin heterogeneity governs nuclear condensate ripening. *bioRxiv*, 2024.05. 07.593010 (2024).

19. Graham, K. *et al*. Liquid-like VASP condensates drive actin polymerization and dynamic bundling. *Nature Physics* **19**, 574-585 (2023).

20. Linsenmeier, M. *et al*. The interface of condensates of the hnRNPA1 low-complexity domain promotes formation of amyloid fibrils. *Nature chemistry* **15**, 1340-1349 (2023).

21. Mangiarotti, A., Chen, N., Zhao, Z., Lipowsky, R. & Dimova, R. Wetting and complex remodeling of membranes by biomolecular condensates. *Nature Communications* **14**, 2809 (2023).

22. Agudo-Canalejo, J. *et al*. Wetting regulates autophagy of phase-separated compartments and the cytosol. *Nature* **591**, 142-146 (2021).

23. Milovanovic, D., Wu, Y., Bian, X. & De Camilli, P. A liquid phase of synapsin and lipid vesicles. *Science* **361**, 604-607 (2018).

24. Snead, W. T. & Gladfelter, A. S. The control centers of biomolecular phase separation: how membrane surfaces, PTMs, and active processes regulate condensation. *Mol. Cell* **76**, 295-305 (2019).

25. Yamasaki, A. *et al*. Liquidity Is a Critical Determinant for Selective Autophagy of Protein Condensates. *Mol. Cell* (2020).

26. Hoffmann, C. *et al*. Synapsin condensation controls synaptic vesicle sequestering and dynamics. *Nature Communications* **14**, 6730 (2023).

27. Pechstein, A. *et al*. Vesicle clustering in a living synapse depends on a synapsin region that mediates phase separation. *Cell Reports* **30**, 2594-2602. e3 (2020).

28. Südhof, T. C. *et al*. Synapsins: mosaics of shared and individual domains in a family of synaptic vesicle phosphoproteins. *Science* **245**, 1474-1480 (1989).

29. Chi, P., Greengard, P. & Ryan, T. A. Synaptic vesicle mobilization is regulated by distinct synapsin I phosphorylation pathways at different frequencies. *Neuron* **38**, 69-78 (2003).

30. Hoffmann, C. *et al*. Synapsin Condensates Recruit alpha-Synuclein. *J. Mol. Biol.*, 166961 (2021).

31. Atias, M. *et al*. Synapsins regulate α-synuclein functions. *Proceedings of the National Academy of Sciences* **116**, 11116-11118 (2019).

32. Stavsky, A. *et al*. Synapsin E-domain is essential for α-synuclein function. *Elife* **12**, RP89687 (2024).

33. Sharma, M. & Burré, J. α-Synuclein in synaptic function and dysfunction. *Trends Neurosci.* **46**, 153-166 (2023).

34. Bendor, J. T., Logan, T. P. & Edwards, R. H. The function of α-synuclein. *Neuron* **79**, 1044-1066 (2013).

35. Jasutkar, H. G., Oh, S. E. & Mouradian, M. M. Therapeutics in the pipeline targeting α-synuclein for Parkinson's disease. *Pharmacol. Rev.* **74**, 207-237 (2022).

36. Vargas, K. J. *et al*. Synucleins have multiple effects on presynaptic architecture. *Cell reports* **18**, 161-173 (2017).

37. Wallace, J. N. *et al*. Excess phosphoserine-129 α-synuclein induces synaptic vesicle trafficking and declustering defects at a vertebrate synapse. *Mol. Biol. Cell* **35**, ar10 (2024).

38. Diao, J. *et al*. Native α-synuclein induces clustering of synaptic-vesicle mimics via binding to phospholipids and synaptobrevin-2/VAMP2. *elife* **2**, e00592 (2013).

39. Nemani, V. M. *et al*. Increased expression of α-synuclein reduces neurotransmitter release by inhibiting synaptic vesicle reclustering after endocytosis. *Neuron* **65**, 66-79 (2010).

40. Wang, H., Kelley, F. M., Milovanovic, D., Schuster, B. S. & Shi, Z. Surface tension and viscosity of protein condensates quantified by micropipette aspiration. *Biophysical Reports*, 100011 (2021).

41. Roggeveen, J. V., Wang, H., Shi, Z. & Stone, H. A. A calibration-free model of micropipette aspiration for measuring properties of protein condensates. *Biophys. J.* (2023).

42. Alshareedah, I., Thurston, G. M. & Banerjee, P. R. Quantifying viscosity and surface tension of multicomponent protein-nucleic acid condensates. *Biophys. J.* (2021).

43. Hamill, O. P., Marty, A., Neher, E., Sakmann, B. & Sigworth, F. J. Improved patch-clamp techniques for high-resolution current recording from cells and cell-free membrane patches. *Pflügers Archiv* **391**, 85-100 (1981).

44. Hosaka, M. & Su□dhof, T. C. Homo-and heterodimerization of synapsins. *J. Biol. Chem.* **274**, 16747-16753 (1999).

45. Kaur, T. *et al*. Molecular crowding tunes material states of ribonucleoprotein condensates. *Biomolecules* **9**, 71 (2019).

46. André, A. A. M., Yewdall, N. A. & Spruijt, E. Crowding-induced phase separation and gelling by co-condensation of PEG in NPM1-rRNA condensates. *Biophysical journal* **122**, 397-407 (2023).

47. Chauhan, G., Bremer, A., Dar, F., Mittag, T. & Pappu, R. V. Crowder titrations enable the quantification of driving forces for macromolecular phase separation. *Biophys. J.* (2023).

48. Qian, D. *et al*. Tie-line analysis reveals interactions driving heteromolecular condensate formation. *Physical Review X* **12**, 041038 (2022).

49. Qiu, H. *et al*. Short-distance vesicle transport via phase separation. *Cell* (2024).

50. Yoshida, T. *et al*. Compartmentalization of soluble endocytic proteins in synaptic vesicle clusters by phase separation. *Iscience* **26** (2023).

51. Scott, D. A. *et al*. A pathologic cascade leading to synaptic dysfunction in α-synuclein-induced neurodegeneration. *Journal of Neuroscience* **30**, 8083-8095 (2010).

52. Hardenberg, M. C. *et al*. Observation of an α-synuclein liquid droplet state and its maturation into Lewy body-like assemblies. *Journal of molecular cell biology*, mjaa075 (2021).

53. Kim, W. S., Kågedal, K. & Halliday, G. M. Alpha-synuclein biology in Lewy body diseases. *Alzheimer's research & therapy* **6**, 1-9 (2014).

54. Twohig, D. & Nielsen, H. M. α-synuclein in the pathophysiology of Alzheimer's disease. *Molecular neurodegeneration* **14**, 1-19 (2019).

55. Ray, S. *et al*. α-Synuclein aggregation nucleates through liquid–liquid phase separation. *Nature Chemistry*, 1-12 (2020).

56. Chemin, J. *et al*. Overexpression of T-type calcium channels in HEK-293 cells increases intracellular calcium without affecting cellular proliferation. *FEBS Lett.* **478**, 166-172 (2000).

57. Dai, Y. *et al*. Interface of biomolecular condensates modulates redox reactions. *Chem*.

58. Hoffmann, C. *et al*. Electric potential at the interface of membraneless organelles gauged by graphene. *Nano letters* **23**, 10796-10801 (2023).

59. Wei, M. *et al*. Phase behaviour of disordered proteins underlying low density and high permeability of liquid organelles. *Nature chemistry* **9**, 1118-1125 (2017).

60. Guevorkian, K., Colbert, M., Durth, M., Dufour, S. & Brochard-Wyart, F. Aspiration of biological viscoelastic drops. *Phys. Rev. Lett.* **104**, 218101 (2010).

61. Zhou, H. Viscoelasticity of biomolecular condensates conforms to the Jeffreys model. *J. Chem. Phys.* **154** (2021).

62. Drury, J. L. & Dembo, M. Hydrodynamics of micropipette aspiration. *Biophys. J.* **76**, 110-128 (1999).

63. Yang, S. *et al*. Membrane curvature governs the distribution of Piezo1 in live cells. *Nature Communications* **13**, 1-14 (2022).

64. Zhang, Y. *et al*. Interface resistance of biomolecular condensates. *eLife* **12**, RP91680 (2023).

65. Riback, J. A. *et al*. Viscoelasticity and advective flow of RNA underlies nucleolar form and function. *Mol. Cell* **83**, 3095-3107. e9 (2023).

66. Kohansal-Nodehi, M., Chua, J. J., Urlaub, H., Jahn, R. & Czernik, D. Analysis of protein phosphorylation in nerve terminal reveals extensive changes in active zone proteins upon exocytosis. *Elife* **5**, e14530 (2016).

67. Chi, P., Greengard, P. & Ryan, T. A. Synapsin dispersion and reclustering during synaptic activity. *Nat. Neurosci.* **4**, 1187-1193 (2001).

68. Ramalingam, N. *et al*. Dynamic physiological α-synuclein S129 phosphorylation is driven by neuronal activity. *npj Parkinson's Disease* **9**, 4 (2023).

69. Parra-Rivas, L. A. *et al*. Serine-129 phosphorylation of α-synuclein is an activity-dependent trigger for physiologic protein-protein interactions and synaptic function. *Neuron* **111**, 4006-4023. e10 (2023).

70. Böddeker, T. J., Rusch, A., Leeners, K., Murrell, M. P. & Dufresne, E. R. Actin and microtubules position stress granules. *PRX Life* **1**, 023010 (2023).

71. Ghosh, A. & Zhou, H. Determinants for Fusion Speed of Biomolecular Droplets. *Angewandte Chemie International Edition* **59**, 20837-20840 (2020).

72. Jackson, J. *et al*. Actin-nucleation promoting factor N-WASP influences alpha-synuclein condensates and pathology. *Cell death & disease* **15**, 304 (2024).

73. Grimm, J. B. *et al*. A general method to improve fluorophores using deuterated auxochromes. *Jacs Au* **1**, 690-696 (2021).

74. Rühl, P. *et al*. Monitoring of compound resting membrane potentials of cell cultures with ratiometric genetically encoded voltage indicators. *Communications Biology* **4**, 1164 (2021).

Methods:

Protein expression and purification

eGFP-synapsin 1

eGFP-synapsin 1 was expressed in Expi293F™cells (Thermo Fisher Scientific) for three days following enhancement and was purified as described previously [23, 30]. In short, cells were lysed in a buffer that contained 25 mM Tris-HCl (pH 7.4), 300 mM NaCl, 0.5 mM TCEP (buffer A) supplemented with EDTA-free Roche Complete protease inhibitors, 25 mM imidazole, 10 µg/mL DNase I and 1 mM $MgCl_2$. All purification steps were carried out at 4°C. Debris was removed by centrifugation for 1 hour at 20,000 x g. For affinity purification, soluble supernatant was applied on a Ni-NTA column (HisTrap™HP, Cytiva, ÄKTA pure 25M) for binding. After a wash step (buffer A with 40 mM imidazole) and elution (buffer A with 400 mM imidazole), proteins were concentrated and subjected to size exclusion chromatography (Superdex™ 200 Increase 10/300, GE Healthcare, ÄKTA pure 25M) in 25 mM Tris-HCl (pH 7.4), 150 mM NaCl, 0.5 mM TCEP. Proteins were snap-frozen in liquid nitrogen and stored at -80 °C until further use.

alpha-Synuclein WT and alpha-synuclein 140C

For condensate partitioning experiments (Figure 3F, 3G, and S3), untagged human alpha-synuclein and alpha -synuclein-A140C were expressed from pET28a vector (Novagen). In brief, a 1 L expression culture (LB; 10 g/L tryptone, 5 g/L yeast extract, 5 g/L NaCl) supplemented with 50 µg/mL kanamycin was inoculated with an overnight preculture to achieve a final OD600 of 0.1. Cells were incubated at 37°C and protein expression was induced at an OD600 of 0.7-0.8 with 1 mM isopropylthio-β-galactoside (IPTG). Cells were shifted to 18°C and incubated overnight while shaking. Upon expression, cells were harvested by centrifugation (7,000xg for 15 min at 4°C).

For alpha-synuclein purification, the pellet was resuspended in 20 mL ice-cold PBS (Gibco 10010015) supplemented with protease inhibitors (Complete EDTA-free, Roche) and a spatula tip of lysozyme (A3711, AppliChem). Suspension was subjected to lysis in a French press. The lysate was cleared by centrifugation (30 min at 50,000xg at 4°C). Nucleic acids were precipitated by adding streptomycin sulfate (S6501, Sigma) to 10 mg/mL final concentration with constant agitation for 30 minutes at room temperature.

For purification of alpha -synuclein-A140C variant 1 mM DTT was added. Subsequently the nucleic acids were pelleted by centrifugation (30 min at 50,000 x g and at 4 °C). The supernatant was transferred to a clean glass beaker and proteins were precipitated by slowly adding ammonium sulfate to a final concentration of 0.36 g/mL with constant agitation for 60 min at 4 °C. Proteins were collected by centrifugation for 30 min at 50,000 x g (4 °C). The pellet was resuspended in 10 mL PBS and boiled for 20 min. After centrifugation (30 min at 50,000 x g, 4 °C), the alpha-synuclein containing supernatant was subjected for dialysis against 5 L of 15 mM Tris base solution overnight (132655T, Spectrum™ Labs Spectra/Por™1 6-8 kDa MWCO Standard RC). For dialysis and subsequent ion exchange

chromatography of alpha-synuclein-A140C variant, 1 mM DTT (final concentration) was used in all steps. The dialyzed protein solution was subjected to anion exchange chromatography (HiPrep Q FF 16/10, Cytiva, ÄKTA pure 25 M) in 25 mM Tris-HCl pH 7.7 (Buffer IEX). Elution was performed stepwise against 25 mM Tris-HCl pH 7.7 containing 500 mM NaCl (IEX-HIGH). First, unwanted material was washed out with 30% IEX-HIGH. Second, alpha-synuclein was eluted with 50% IEX-HIGH (= 250 mM NaCl). Elution fractions were analyzed by SDS-PAGE (18% gel). Fractions containing alpha-synuclein were concentrated (Amicon® Ultra 4 MWCo 3kD, Merck Millipore) and subjected to size exclusion chromatography (Superdex™ 200 Increase 10/300, GE Healthcare, ÄKTA pure 25M) in 25 mM Tris-HCl (pH 7.4), 150 mM NaCl, 0.5 mM TCEP. alpha-synuclein concentration was determined at 280 nm by using a molar extinction coefficient of 5960 M^{-1} cm^{-1}. Proteins were snap-frozen in liquid nitrogen and stored at -80 °C until further use.

For MPA measurements (Figure 3A – 3E, S2C, S2D), alpha-synuclein was expressed using the pT7-7 aSyn WT vector (Addgene #36046) in BL21(DE3) bacteria (NEB). Briefly, 50mL starter cultures of LB media (Fisher Scientific, BP1426-2) with 50mg/mL ampicillin (Fisher Scientific, BP1760), were inoculated with freshly picked colonies and grown overnight (37°C, 160RPM). The starter cultures were used to inoculate 1L flasks of fresh LB with ampicillin and grown at 37°C (180RPM) until the OD600 measured 0.6-0.8. Expression was induced with 1mM isopropylthio-β-galactoside (IPTG; Teknova I3325) and grown in the incubator overnight (20°C, 160RPM), after which cells were subsequently harvested by centrifugation (4000 rpm, 4°C, 30 minutes) and stored at -80°C until use.

alpha-Synuclein-A140C was generated from the pT7-7 aSyn WT vector using the Q5 Site-Directed Mutagenesis Kit (NEB, E0554) according to manufacturer's instructions. Primers were designed using the NEBaseChanger tool and the sequences used were as follows: 5'-CGAACCTGAATGCTAAGAAATATCTTTGC-3' and 5'- TAGTCTTGATACCCTTCC-3'.

alpha-Synuclein purification was accomplished by suspension of the bacterial pellet in fresh PBS (Fisher Scientific, BP2944), followed by sonication on ice (15 sec on, 30 sec off; 8 cycles total). The solution was then boiled, followed by centrifugation to clear the lysate (20,000 rpm, 4 °C, 30 minutes). Streptomycin sulfate (Fisher Scientific, BP910-50) was added to the supernatant to a final concentration of 10mg/mL and mixed at 4°C for 30 minutes, followed by centrifugation using the same conditions as before. The protein was precipitated from the supernatant by adding ammonium sulfate (Fisher Scientific, BP212-212) to a final concentration of 0.361G/mL and mixing at 4°C for 1 hour. The protein was pelleted by centrifugation, and the protein pellet was resuspended in buffer A (32.2mM Tris Base, pH 7.8). alpha-Synuclein was purified via FPLC (Cytiva A□KTA Pure) using HiTrap Q HP anion exchange columns (Cytiva) and eluted at 50% buffer B (32.2mM Tris Base, 500mM NaCl, pH 7.8). Final proteins were aliquoted, flash frozen in liquid nitrogen, and stored at -80°C until use. alpha-Synuclein A140C was purified in the same way as described above, but with the addition of 1mM DTT.

To label alpha-synuclein-A140C, first, the protein solution was centrifuged at 16,000 g for 30 minutes with a 3 kD cut-off filter (Amicon Ultra Centrifugal Filter, 3 kDa MWCO, Merck Millipore) to remove previous buffer. The centrifugation step was repeated, when necessary,

to reach a targeted protein concentration of 2 mg/ml in PBS. Next, the protein solution was centrifuged at 16, 000 g for 10 minutes with a 100 kD cut-off filter (Amicon Ultra Centrifugal Filter, 100 kDa MWCO, Merck Millipore) to remove potential protein aggregations. Then, the protein solution was incubated with 2x excess Alexa Fluor™ 647 C2 Maleimide (Invitrogen™) for 2 h at room temperature. Next, the protein dye mixture was passed through a desalting column (Zeba Spin Desalting Columns, Thermo Scientific) to remove excess dye. The concentration of labelled protein and degree of labelling were determined by Nanodrop (Invitrogen™ Nanodrop™ One, Fisher scientific).

Preparation of synaptic vesicles

Synaptic vesicles (SVs) were isolated according to previous publications [30]. Briefly, 20 rat brains were homogenized in ice-cold sucrose buffer (320 mM sucrose, 4 mM HEPES-KOH, pH 7.4 supplemented with 0.2 mM phenylmethylsulfonylfluoride and 1 mg/ml pepstatin A). Debris was removed by centrifugation (10 min at 900 gAv, 4 °C) and the resulting supernatant was further centrifuged (10 min at 12,000 gAv, 4 °C). The pellet containing synaptosomes was washed once, and synaptosomes were lysed by hypo-osmotic shock. Free, released SVs were obtained after centrifugation of the lysate for 20 min at 20,000 gAv, 4 °C. The supernatant containing the SVs was further ultracentrifuged for 2 h at 230,000 gAv, resulting in a crude synaptic vesicle pellet. Subsequently, SVs were purified by resuspending the pellet in 40 mM sucrose followed by centrifugation for 3 h at 110,880 gAv on a continuous sucrose density gradient (50–800 mM sucrose). SVs were collected from the gradient and loaded to size-exclusion chromatography on glass beads (300 nm diameter), equilibrated in glycine buffer (300 mM glycine, 5 mM HEPES, pH 7.40, adjusted using KOH). This allows for the separation of synaptic vesicles from residual larger membrane contaminants. SVs were pelleted by centrifugation for 2 h at 230,000 gAv and resuspended in sucrose buffer by homogenization before being aliquoted into single-use fractions and snap-frozen in liquid nitrogen until use.

Condensate fusion experiments

An optical tweezers-assisted fusion assay was carried out and analyzed following the protocol we previously described [40]. Two condensates were independently trapped by a pair of separate optical tweezers at minimal power (Tweez305, Aresis, Slovenia; mounted on a Nikon Ti2-A inverted microscope). The fusion events were captured at 20 Hz with a 60x water objective. MATLAB R2020b was used to analyze the captured images. The images were fitted to a Gaussian ellipse. The aspect ratio (*AR*), which is the ratio between the major and minor axes of the ellipse, was plotted over time (Figure 1B). The time of fusion τ_{fusion} was deduced by fitting the relaxation in *AR* to a stretched exponential decay [71].

$$AR = (AR_0 - 1)\mathrm{e}^{\left(-\frac{t}{\tau_{\mathrm{fusion}}}\right)^{1.5}} + 1$$

The condensates' length was designated as the geometric mean of the condensate diameters prior to fusion. The ratio of viscosity over interfacial tension was calculated from the slope of the fusion time vs. length (Figure 1C).

MPA experiments in vitro

The micropipette aspiration experiments were carried out on a Ti2-A inverted fluorescence microscope (Nikon, Japan) equipped with a motorized stage and two motorized 4-axes micromanipulators (PatchPro-5000, Scientifica) and a multi-trap optical tweezers (Tweez305, Aresis, Slovenia) according to the protocol we reported previously [40] with minor modifications.

Micropipettes were made by pulling glass capillaries using a pipette puller (PUL-1000, World Precision Instruments). The pipette tip was then cut to achieve an opening diameter ranging from 2 to 5 μm. Subsequently, the pipette was bent to an angle of approximately 40° using a microforge (DMF1000, World Precision Instruments).

The micropipette was filled with the same buffer as the buffer for synapsin (25 mM Tris-HCl, 150 mM NaCl, 0.5 mM TCEP, pH = 7.4) using a MICROFIL needle (World Precision Instruments). The filled micropipette was then mounted onto a micromanipulator. The rear end of the pipette was connected to an automatic pressure controller (Flow-EZ, Fluigent; Pressure resolution 1 Pa). The MPA experiments were conducted in glass-bottom dishes (D35-20-1.5-N, Cellvis), under brightfield illumination to minimize potential artifacts associated with fluorescence excitation. Fluorescence images were taken after MPA experiment to confirm the protein species. Typically, optical tweezers-assisted condensate fusion experiments were first carried out to achieve a large (> 5 μm) condensate for easier MPA measurements and analysis. A secondary micropipette was used to hold the condensate during MPA. To minimize sample evaporation, 1.5 mL Milli-Q water was added to the edge of the dish, and the dishes were covered with a thin plastic wrap with a ~2 mm hole for pipette insertion.

We observed that in vitro synapsin condensates always wet the inner wall of uncoated micropipettes. Therefore, the analysis of the MPA data (e.g., Figure 1D-1H) follows the protocol described in reference [41]. Briefly, normalized aspiration length (L_p/R_p) was segmented according to the pressure steps. For each segment, the slope of a linear fitting of $(L_p/R_p)^2$ vs. time gives the effective shear rate S. Then the slope of P_{asp} vs. S gives the 4η, the intercept gives $2\gamma/R_p$.

Condensate partitioning measurement

For in vitro partitioning measurements (Figure 3F, 3G, and S3), eGFP-synapsin 1, Polyethylene glycol 8,000 (PEG 8,000), sample buffer, and (if required) maleimide-labeled alpha-synuclein(A140C)-647 were mixed in a reaction tube (10 μl final volume). From there, the sample was pipetted onto a glass bottom microscopy dish for imaging immediately. The sample solution consisted of 5 μM eGFP-synapsin 1, 3% PEG 8,000, 150 mM NaCl, 25 mM Tris-HCl, 0.5 mM TCEP, pH 7.4 with varying concentrations of alpha-synuclein(A140C)-647 as indicated in the text and the corresponding figures. Each condition was assessed in at least three independent reconstitutions.

The microscopy data was acquired at the Advanced Biomedical Imaging (AMBIO) Facility at Charité Medical Center, using the Eclipse Ti Nikon Spinning Disk Confocal CSU-X,

equipped with 2 EM-CCD cameras (AndorR iXon 888-U3 ultra EM-CCD), Andor Revolution SD System (CSU-X), objectives PL APO 60/1.4NA oil immersion lens. Z-stacks (step-size: 0.3 µm) were acquired with piezo stage z-motor at two different wavelengths (488 nm for eGFP-synapsin 1 and 638 nm for alpha-synuclein(A140C)-647) after loading the sample onto the surface of the microscopy dish over a duration of 15 minutes over a duration of 15 minutes. Each z-series was imaged twice at two different laser intensities. The lower intensity was always used for the analysis. The Exposure times were set to 200 ms (488 nm) and 100 ms (638 nm), and the EM Gain (30 MHz at 16-bit) Multiplier was set to 300 during all these experiments. NIS Elements 5.21.02 software was used to acquire the microscopy data. Fiji ImageJ (NIH) was used to analyze the data.

For the diameter analysis, the equatorial z-plane of most condensates was selected. Then, the area (μm^2) of all condensates within 60 µm of the edge of the sample solution was quantified by applying a Gaussian Blur (Sigma: 2.00 px) and generating a binary image using the Otsu algorithm, based on the images from the synapsin channel. Only particles with a circularity $\geq$ 0.9 were included in the analysis. The diameter of the analyzed condensates was calculated based on the measured area.

For the analysis of the raw and relative fluorescence intensities (partitioning coefficient), a squared section of approximately 40 µm × 40 µm was generated, and the equatorial z-plane was chosen for analysis. Here, the regions of interest (ROIs) were selected by applying a Gaussian blur (Sigma: 2.00 px) and generating a binary image using the Otsu algorithm, based on the images from the synapsin channel, only including particles with a circularity $\geq$ 0.9 in the analysis. Then, ten additional ROIs of similar size to the condensates were placed in the dilute phase on the same z-plane, and the mean fluorescent intensities for each ROI (both condensates and dilute phase) were measured at both wavelengths. A correction value, accounting for the background fluorescence detected by the camera in the absence of any fluorophore, was subtracted from every readout value, and the mean corrected fluorescence intensities were calculated for both channels in the condensates and the dilute phase. The partitioning coefficients for both proteins were computed by dividing each condensate's corrected mean fluorescence intensity by the mean corrected fluorescence intensity in the dilute phase for the same corresponding image.

For the partitioning coefficient of cellular condensates, first confocal and widefield fluorescence images of the same condensate-containing HEK 293T cells were taken on a Zeiss Axio Observer 7 inverted microscope equipped with an LSM900 laser scanning confocal module and using a 63×/1.4 NA plan-apochromatic, oil-immersion objective.

The images were then analyzed using ImageJ. As shown in Figure S10a, the condensate partitioning coefficient (Π) is defined as the background-corrected mean fluorescence of in the condensate ($I_{condensate}$) divided by the background-corrected mean fluorescence of the surrounding cytosol ($I_{cytosol}$) for the studied proteins. The background was measured as the mean extracellular fluorescence.

$$\Pi = \frac{I_{\text{condensate}} - I_{\text{background}}}{I_{\text{cytosol}} - I_{\text{background}}}$$

The partitioning coefficients measured with confocal and widefield microscopy for the same condensates were used to establish a conversion function between Π_{confocal} and $\Pi_{\text{widefield}}$ (Figure S10B). The conversion function ($\Pi_{\text{confocal}} = 6.7\Pi_{\text{widefield}} - 5.7$) was used to assign pseudo-confocal partitioning coefficients on condensates measured in MAPAC with a widefield configuration.

Cell culture and transfection

HEK 293T cells (ATCC) were grown in Dulbecco's Modified Eagle Medium (11995065, Thermo Fisher) enriched with 10% Fetal Bovine Serum (FB12999102, Fisherbrand), 1% Penicillin-Streptomycin (15140122, Thermo Fisher). Approximately 1 million cells were seeded into a 100 mm plastic dish. The cells were maintained in an environment at 37°C, with 5 – 10 % CO^2, and 100% relative humidity.

300,000 cells were seeded onto a 35 mm glass bottom dish (D35-20-1.5-N, Cellvis) precoated with Matrigel Matrix (47743-715-EA, Corning Life Sciences) for transfection. 24 hours after seeding the cell, a mixture of 250µL Opti-MEM, 5 µL P3000 reagent, 7.5 µL Lipofectamine reagent, 1.5 µg of mCherry-Synapsin 1 plasmid [30], and 1 µg alpha-synuclein-Halo [72] or alpha-synuclein-BFP [30] plasmid was added to the dish. Imaging and MAPAC experiments were done 24 hours after transfection. Prior to imaging, Halo-alpha-synuclein expressing cells were incubated with 1 µM JFX-646 Halo Tag Ligand [73] for 15 min, and the cell culture medium was replaced with an extracellular imaging buffer (XC buffer). The XC buffer contained 140 mM NaCl, 5 mM KCl, 10 mM HEPES, 10 mM Glucose, 2mM MgCl2, and 2 mM CaCl2, at a pH of 7.4. All chemicals were ordered from Sigma.

MAPAC experiments

Different from MPA measurements in vitro, micropipettes used in MAPAC were pulled into a cylindrical tip with an opening diameter of 0.5 ~ 1 µm (PUL-1000, World Precision Instruments). The tip was then bent to an angle of approximately 40° using a microforge (DMF1000, World Precision Instruments). The micropipette was filled with an intracellular buffer (126 mM K-Gluconate, 4 mM KCl, 10 mM HEPES, 2 mM Mg-ATP, 0.3 mM Na2-GTP, 10 mM Phosphocreatine, final pH 7.2, osmolarity 270 – 290 mOsm; all chemicals were ordered form Sigma) and mounted to a headstage that is connected to an Axon 700B amplifier (Molecular Devices) and to a home-made pressure recording device using an Arduino(UNO R3,ELEGOO) controlled pressure sensor (B07N8SX347, FTVOGUE, resolution 100 Pa). The micropipette was then inserted into a dish with HEK 293T cells expressing fluorescently labeled condensates under the voltage clamp mode. Typical resistance of the micropipette was 50 MΩ. A small ejection pressure (~ -1 kPa) was applied to the micropipette until the pipette tip reached the targeted cell. Then a suction pressure was maintained in the micropipette to form a giga seal near a targeted condensate. Next, the electrical recording was switched to current clamp mode (with I = 0) and sudden suction pressures pulses >10 kPa were applied to break into the cell. After successfully broke into the cell, the resting membrane voltage was recorded. On healthy HEK 293T cells, reported resting membrane

voltage are around -40mV [74]. To characterize condensate properties under whole-cell patch clamp mode, suction pressures were applied so that the nearby condensate could flow into the tip of the micropipette for subsequent measurements of condensate material properties. Liquid junction potentials were not compensated for in reported cell membrane potential measurements. The voltage recordings were processed through a 2 kHz filter, digitized at a rate of 10 kHz, and collected using Clampex 10.2 software (Molecular Devices).

Acknowledgments:

We thank Drs. James Roggeveen, Howard Stone, Conor McClenaghan, Che-Yu Lin, Benjamin Schuster, Cliff Brangwynne, Wilma Olson, Sagar Khare, and members of the Rutgers LLPS journal club for helpful discussions. We thank Dr. Benjamin Schuster lab for access to confocal microscopy. We thank Dr. Luke Lavis lab for sharing JFX dyes. The project is supported by the National Institute of General Medical Sciences of the National Institutes of Health (NIH) under Award Number R35GM147027 (Z.S.) and by the National Institute on Drug Abuse, the National Institute of Neurological Disorders and Stroke, and the National Institute of Mental Health of the NIH under Award Number R21DA056322 (Z.S.). D.M. is supported by the start-up funds from DZNE, the research grant from the German Research Foundation (MI 2104), and the European Research Council (MEMLESSINTERFACE, 101078172); views and opinions expressed are however those of the authors only and do not necessarily reflect those of the European Union or the European Research Council Executive Agency; neither the European Union nor the granting authority can be held responsible for them. J. B. acknowledges NIH grant: R35GM136431. Z.P.P. acknowledges NIH grant: R21MH126420. C.H. is supported by a fellowship of the Innovative Minds Program of the German Dementia Association. X.S. is supported by a Predoctoral Fellowship from the Autism Science Foundation. The Child Health Institute of New Jersey is partially funded by the Robert Wood Johnson Foundation (RWJF #74260).

Author contribution:

Z.S., D.M. and Huan W. conceived the idea and designed the experiments. Huan W. performed most of the experiments. Huan W. and Z.S. analyzed the data. C.H. and Han W. purified synapsin proteins, synaptic vesicles, alpha-synuclein for in vitro partitioning measurements, and cloned plasmids for live cell experiments. J.V.T. and C.H. performed the experiments in Figure 3F, 3G, and S3. Z.P.P. and X.S. guided

the electrophysiology experiments. J.B. and J.E. designed and purified alpha-synuclein proteins for MPA. Huan W., Z.S., C. H., and D.M. wrote the manuscript with input from all authors.

Competing interests

The authors declare no competing interests.

Figure 1

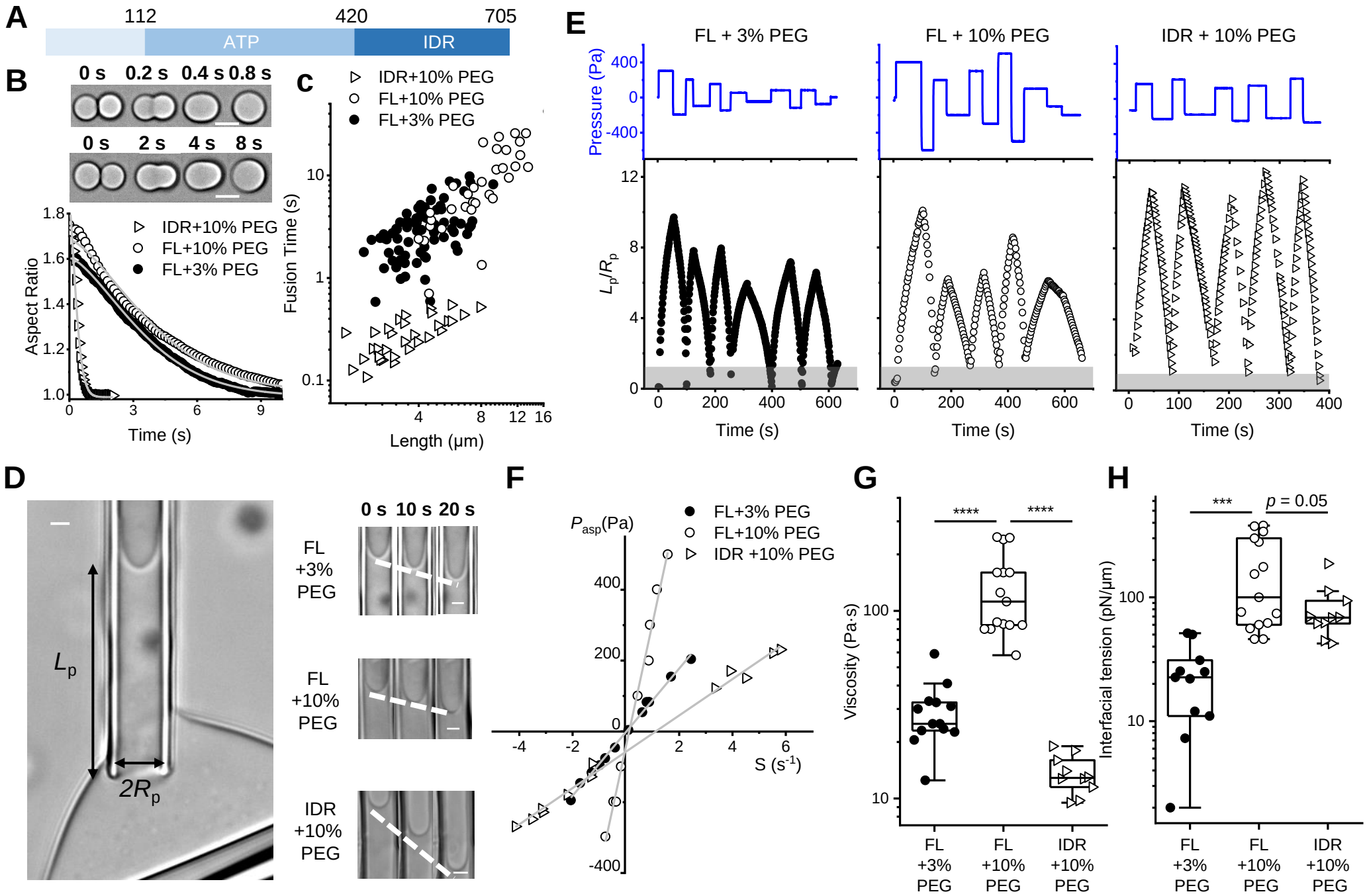
A
112
420
705
ATP
IDR
B
0 s 0.2 s 0.4 s 0.8 s
0 s 2 s 4 s 8 s
IDR+10% PEG
FL+10% PEG
FL+3% PEG
Aspect Ratio
Time (s)
C
IDR+10% PEG
FL+10% PEG
FL+3% PEG
Fusion Time (s)
Length (μm)
E
FL + 3% PEG
FL + 10% PEG
IDR + 10% PEG
Pressure (Pa)
L_p/R_p
Time (s)
D
L_p
$2R_p$
0 s 10 s 20 s
FL +3% PEG
FL +10% PEG
IDR +10% PEG
F
P_{asp}(Pa)
FL+3% PEG
FL+10% PEG
IDR +10% PEG
S (s^{-1})
G
Viscosity (Pa·s)
****
****
FL +3% PEG
FL +10% PEG
IDR +10% PEG
H
Interfacial tension (pN/μm)
***
p = 0.05
FL +3% PEG
FL +10% PEG
IDR +10% PEG

Figure 2

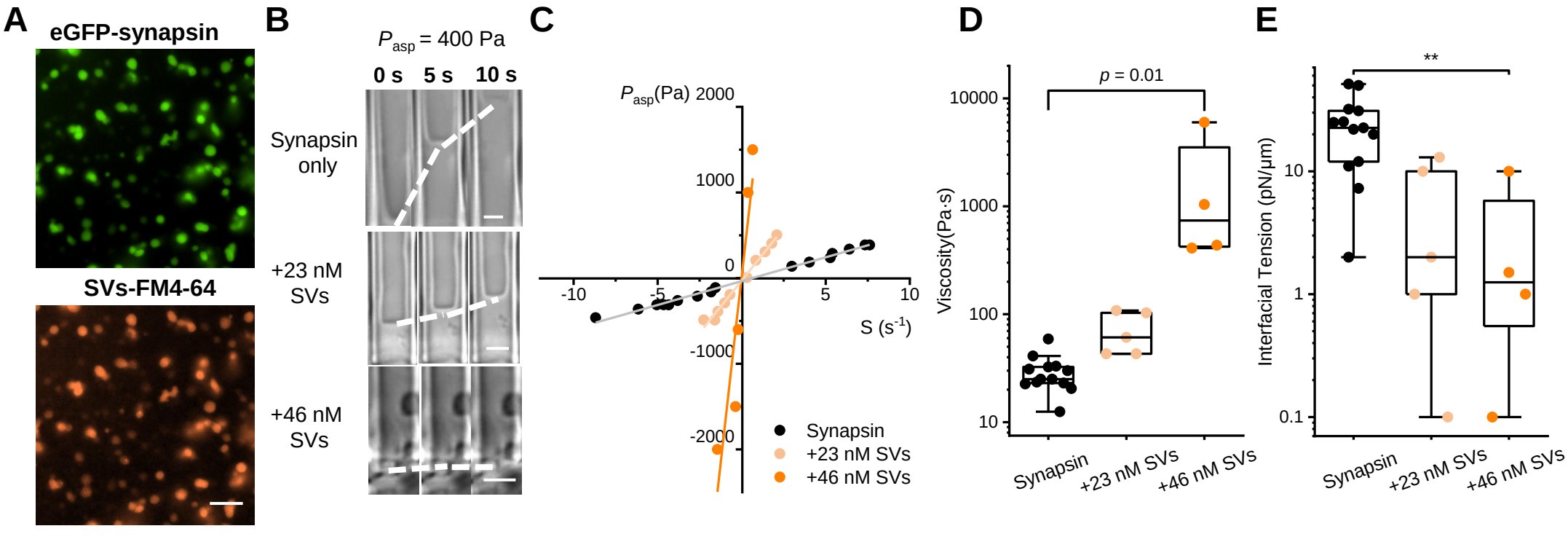
A
eGFP-synapsin
SVs-FM4-64
B
P_{asp} = 400 Pa
0 s
5 s
10 s
Synapsin only
+23 nM SVs
+46 nM SVs
C
P_{asp}(Pa)
2000
1000
0
-1000
-2000
-10
-5
5
10
S (s^{-1})
Synapsin
+23 nM SVs
+46 nM SVs
D
p = 0.01
Viscosity(Pa·s)
10000
1000
100
10
Synapsin
+23 nM SVs
+46 nM SVs
E
**
Interfacial Tension (pN/µm)
10
1
0.1
Synapsin
+23 nM SVs
+46 nM SVs

Figure 3

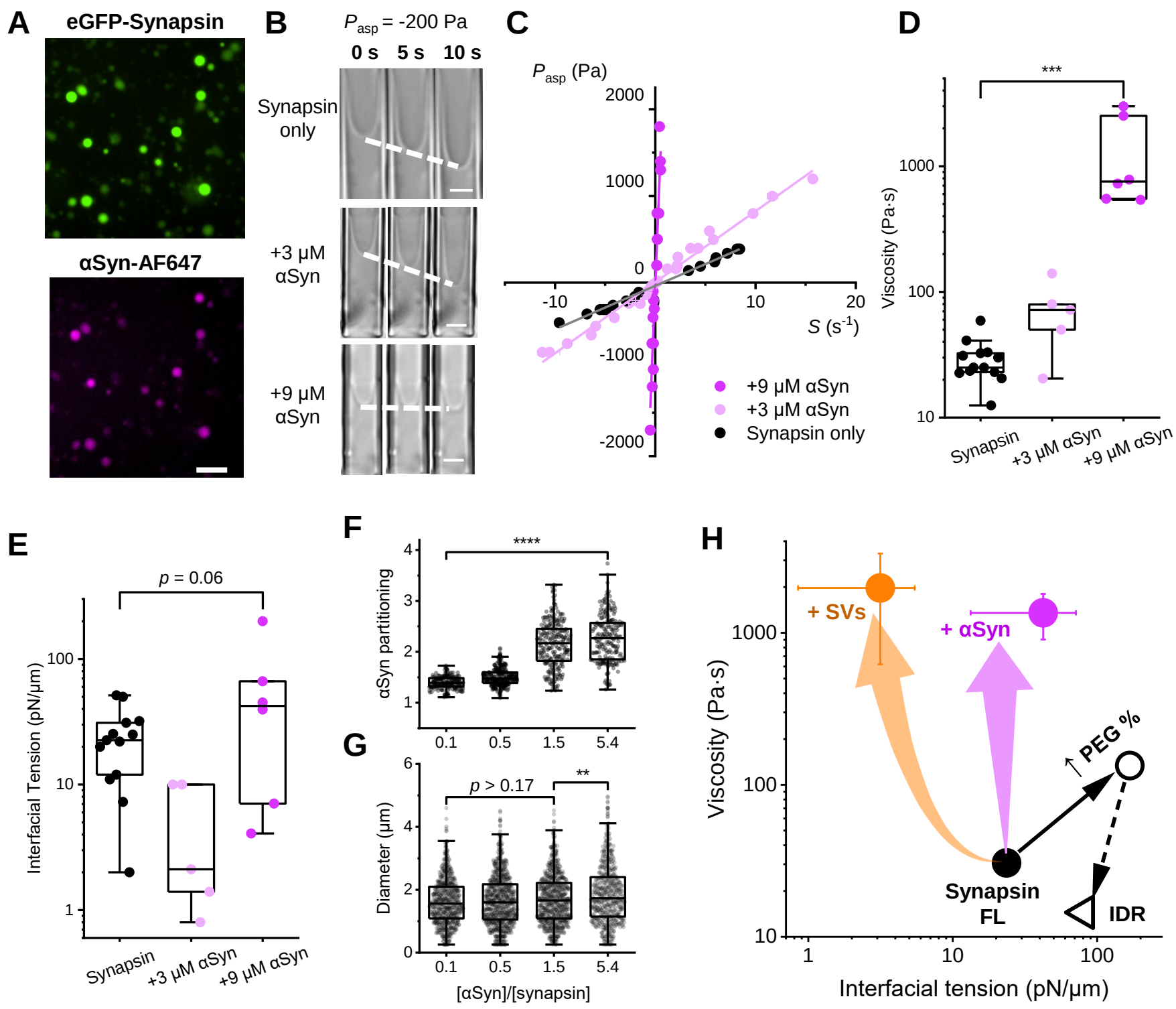
A
eGFP-Synapsin
αSyn-AF647
B
P_{asp} = -200 Pa
0 s
5 s
10 s
Synapsin only
+3 μM αSyn
+9 μM αSyn
C
P_{asp} (Pa)
2000
1000
0
-1000
-2000
-10
10
20
S (s^{-1})
+9 μM αSyn
+3 μM αSyn
Synapsin only
D
***
Viscosity (Pa·s)
1000
100
10
Synapsin
+3 μM αSyn
+9 μM αSyn
E
p = 0.06
Interfacial Tension (pN/μm)
100
10
1
Synapsin
+3 μM αSyn
+9 μM αSyn
F
****
αSyn partitioning
4
3
2
1
0.1
0.5
1.5
5.4
G
p > 0.17
**
Diameter (μm)
6
4
2
0
0.1
0.5
1.5
5.4
[αSyn]/[synapsin]
H
+ SVs
+ αSyn
↑ PEG %
Synapsin FL
IDR
Viscosity (Pa·s)
1000
100
10
1
10
100
Interfacial tension (pN/μm)

Figure 4

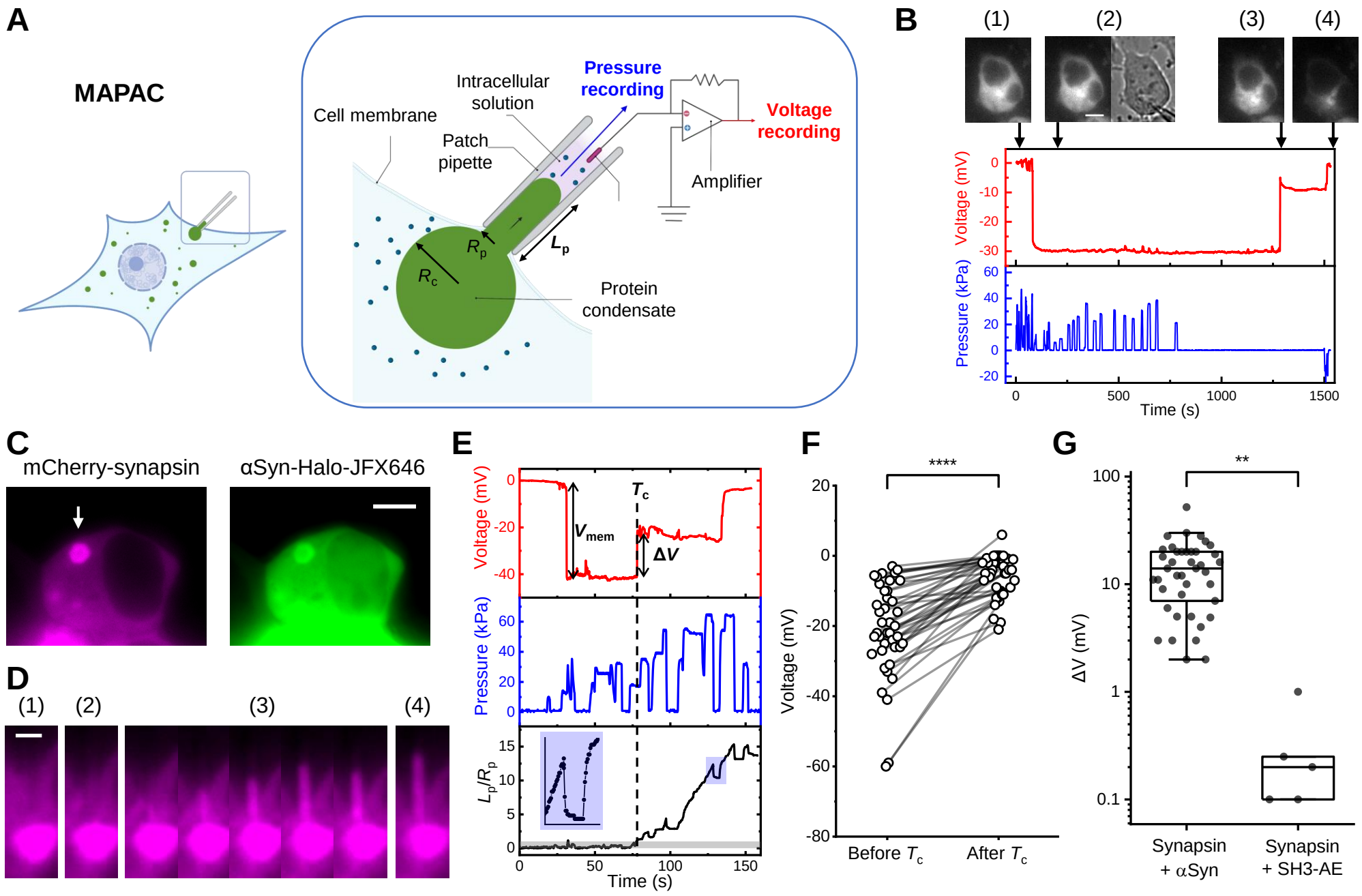
A
MAPAC
Cell membrane
Intracellular solution
Patch pipette
Pressure recording
Voltage recording
Amplifier
R_p
L_p
R_c
Protein condensate
B
(1)
(2)
(3)
(4)
Voltage (mV)
Pressure (kPa)
Time (s)
C
mCherry-synapsin
αSyn-Halo-JFX646
D
(1)
(2)
(3)
(4)
E
Voltage (mV)
V_{mem}
T_c
ΔV
Pressure (kPa)
L_p/R_p
Time (s)
F
****
Voltage (mV)
Before T_c
After T_c
G
**
ΔV (mV)
Synapsin + αSyn
Synapsin + SH3-AE

Figure 5

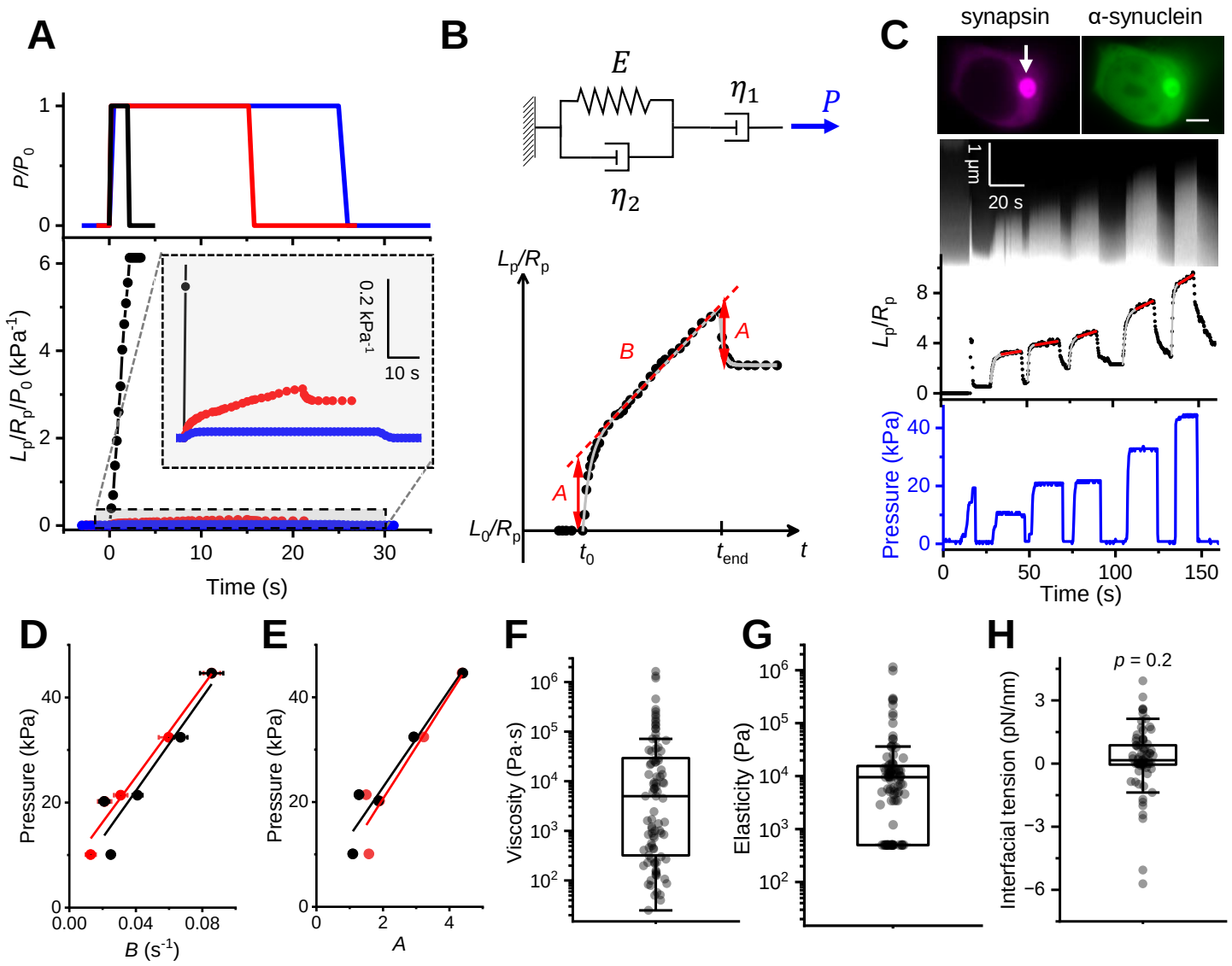
A
P/P0
Lp/Rp/P0 (kPa-1)
0.2 kPa-1
10 s
Time (s)
B
E
η1
η2
P
Lp/Rp
L0/Rp
A
B
t0
tend
t
C
synapsin
α-synuclein
1 μm
20 s
Lp/Rp
Pressure (kPa)
Time (s)
D
Pressure (kPa)
B (s-1)
E
Pressure (kPa)
A
F
Viscosity (Pa·s)
G
Elasticity (Pa)
H
p = 0.2
Interfacial tension (pN/nm)

Figure 6

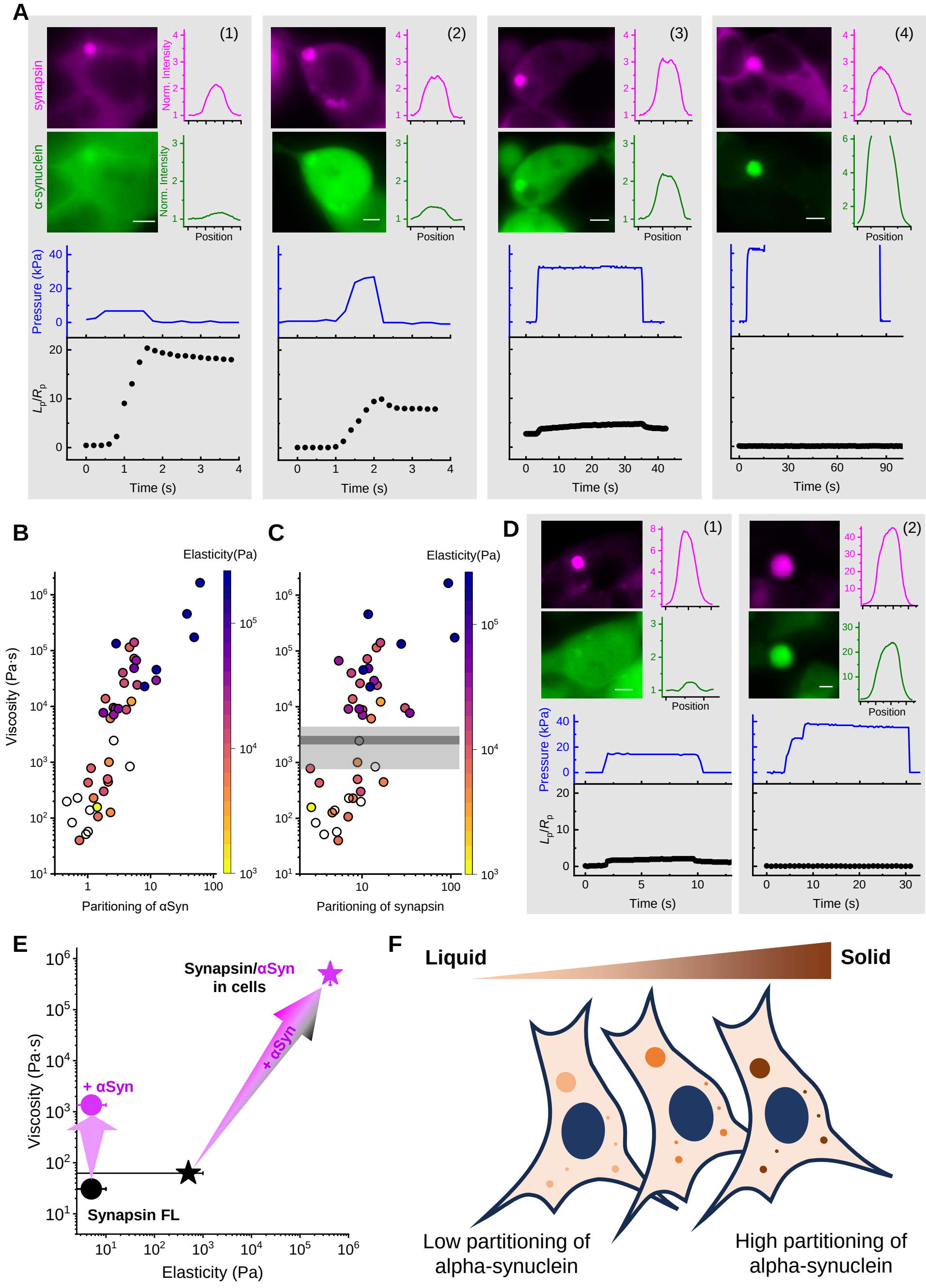
A
(1)
(2)
(3)
(4)
synapsin
α-synuclein
Norm. Intensity
Position
Pressure (kPa)
L_p/R_p
Time (s)
B
Elasticity(Pa)
Viscosity (Pa·s)
Paritioning of αSyn
C
Paritioning of synapsin
D
E
Synapsin/αSyn in cells
+ αSyn
Synapsin FL
Elasticity (Pa)
F
Liquid
Solid
Low partitioning of alpha-synuclein
High partitioning of alpha-synuclein